3D MAGNETOTELLURIC CHARACTERIZATION OF THE COSO GEOTHERMAL FIELD

APRIL 23, 2007

Gregory A. Newman, G. Michael Hoversten[#], Philip E. Wannamaker[+] and Erika Gasperikova**

**Lawrence Berkeley National Laboratory, Earth Sciences Division*
1 Cyclotron Road, Berkeley CA, 94720
e-mail:ganewman@lbl.gov

[#] Chevron Energy Technology Company
Seismic Analysis & Property Estimation
6001 Bollinger Canyon Rd, D1046
San Ramon CA, 94583

[+]University of Utah/Energy & Geoscience Institute
423 Wakara Way, Suite 300
Salt Lake City, UT 84108

ABSTRACT

Electrical resistivity may contribute to progress in understanding geothermal systems by imaging the geometry, bounds and controlling structures in existing production, and thereby perhaps suggesting new areas for field expansion. To these ends, a dense grid of magnetotelluric (MT) stations plus a single line of contiguous bipole array profiling has been acquired over the east flank of the Coso geothermal system. Acquiring good quality MT data in producing geothermal systems is a challenge due to production related electromagnetic (EM) noise and, in the case of Coso, due to proximity of a regional DC intertie power transmission line. To achieve good results, a remote reference completely outside the influence of the dominant source of EM noise must be established. Experimental results so far indicate that emplacing a reference site in Amargosa Valley, NV, 65 miles from the DC intertie, is still insufficient for noise cancellation much of the time. Even though the DC line EM fields are planar at this distance, they remain coherent with the nonplanar fields in the Coso area hence remote referencing produces incorrect responses. We have successfully unwrapped and applied MT times series from the permanent observatory at Parkfield, CA, and these appear adequate to suppress the interference of the cultural EM noise. The efficacy of this observatory is confirmed by comparison to stations taken using an ultra-distant reference site east of Socorro, NM. Operation of the latter reference was successful by using fast ftp internet communication between Coso Junction and the New Mexico Institute of Mining and Technology, using the University of Utah site as intermediary, and allowed referencing within a few hours of data downloading at Coso.

A grid of 102 MT stations was acquired over the Coso geothermal area in 2003 and an additional 23 stations were acquired to augment coverage in the southern flank of the first survey area in 2005. These data have been inverted to a fully three-dimensional conductivity model. Initial analysis of the Coso MT data was carried out using 2D MT imaging. An initial 3D conductivity model was constructed from a series of 2D resistivity images obtained using the inline electric field measurements (Z_{yx} impedance elements) along several measurement transects. This model was then refined through a 3D inversion process. This model shows the controlling geological structures possibly influencing well production at Coso and correlations with mapped surface features such as faults and regional geoelectric strike. The 3D model also illustrates the refinement in positioning of conductivity contacts when compared to isolated 2D inversion transects. The conductivity model has also been correlated with microearthquake locations, well fluid production intervals and most importantly with an acoustic and shear velocity model derived by Wu and Lees (1999). This later correlation shows the near-vertical high conductivity structure on the eastern flank of the producing field is also a zone of increased acoustic velocity and increased Vp/Vs ratio bounded by mapped fault traces. South of the Devils' Kitchen is an area of high geothermal well density, where highly conductive near surface material is interpreted as a clay cap alteration zone manifested from the subsurface geothermal fluids and related geochemistry. Beneath the clay cap, however, the conductivity is nondescript, whereas the Vp/Vs ratio is enhanced over the production intervals. It is recommended that more MT data sites be acquired to the southwest of the Devil's Kitchen area to better refine the conductivity model in that area.

INTRODUCTION

A critical component in understanding the hydrothermal properties of complex geothermal reservoirs, typical of the Coso geothermal field, is technology to provide images of subsurface structures, which control geothermal fluid flow. A range of geophysical techniques can be used to image variations in the bulk geophysical properties of rocks. These bulk properties are limited in number, but the most common are seismic velocity (acoustic and shear), density and electrical conductivity (the reciprocal of resistivity).

The degree to which a geophysical technique can be used successfully to infer geothermal reservoir properties (fracture orientation, fracture density, temperature and fluid saturations) depends on how uniquely the reservoir parameters are related to the geophysical parameters. Because these relationships are often not unique (high water saturation and high clay content both produce high electrical conductivity) it may be necessary to integrate multiple geophysical techniques to better interpret reservoir parameters from geophysical data. In this paper we describe the application of magnetotellurics (MT) at the Coso geothermal field and show the correlations (or lack there of) between the derived electrical parameters and seismic velocity from other experiments.

MT has a long history in geothermal exploration. With the recent advent of distributed computing, realistic 3D MT modeling and inversion has emerged as a promising technique to model and image the electrical structure of geothermal reservoirs in a single self consistent manner at presumably optimal accuracy and resolution. We will test this assumption on MT data acquired over the eastern and southern flank of the Coso geothermal field and investigate whether 3D modeling and imaging can avoid artifacts possible in 2D data analysis. Demonstrating this in the geothermal context may push MT characterization of geothermal systems beyond the current state and may provide additional value added information in geothermal well positioning

COSO FIELD GEOLOGICAL SETTING

The Coso Geothermal area (Figure 1) is located in the Coso Range at the margin between the eastern flank of the Sierra Nevada and the western edge of the Basin and Range tectonic province of southeastern California, and lies within the Walker Lane/Eastern California Shear Zone (WLSZ). The Basin and Range province, an area of high heat flow and seismicity, is characterized by northerly trending fault block mountains separated by alluvial valleys that result from extensional tectonism. The Walker Lane/Eastern California Shear Zone is a tectonically active feature and is characterized in this region as accommodating approximately 11 mm/yr of north-south trending, right-lateral strike-slip motion between "stable North America" and the Sierra Nevada (McClusky et al., 2000). To the west, the Coso Range is separated from the Sierra Nevada by Rose Valley, the southern extension of the Owens Valley. It is bounded to the North by Owens Lake, a large saline playa. On the east, the range is bounded by Darwin (Coso) Wash and the Argus Range, and on the south by Indian Wells Valley.

The Coso Range basement is dominated by fractured Mesozoic plutonic with minor metamorphic rocks that have been intruded and partly covered by late Cenozoic volcanic rocks. The basement complex has been intruded by a large number of northwest trending, fine-grained dikes. These dikes range in composition from felsic to mafic rocks and are believed to be part of the Independence Dike swarm of Cretaceous age. The late Cenozoic volcanic rocks consist of basalts and rhyolites. In the most recent volcanic phase, thirty-nine rhyolite domes were emplaced since 1 Ma in the central region of the field along with a relatively small amount of basalt on the margins. Over the past 0.6 My, the depth from which the rhyolites erupted has decreased, ranging from ~10 km depth for the ~0.6 Ma magma, to ~5.5 km for the youngest (~0.04 Ma) magma. These results can be explained by either a single rhyolitic reservoir moving upward through the crust, or a series of successively shallower reservoirs, consistent with the recent Ar-Ar geochronology (Kurilovitch et al., 2003). As the reservoir has become closer to the surface, eruptions have become both more frequent and more voluminous (Manley and Bacon, 2000). This partially molten magma chamber is believed to be the heat source that drives the geothermal system.

Stresses that control the faulting and fracture permeability of the reservoir rocks are believed to be the result of the location of the Coso Range in the transitional zone between Basin and Range extensional tectonics to the east and strike-slip tectonics to the west (Roquemore, 1980; McClusky *et al*, 2000). Two major fault orientations have been recognized to control the geothermal system. The first set of faults strike WNW, have a vertical dip, and have strike-slip earthquake solutions, while the other strongly developed system of faults strike NNE and dip to the east. The NNE striking fault zones have been successfully targeted in development of the Coso geothermal field, in particular in the east flank area where wells drilled with a steep westerly dip have been the most productive (e.g., Sheridan et al., 2003). Permeability is high within the individual Coso reservoirs (i.e., Figure 1) but low in most of the surrounding rock. This limits recharge to the reservoir and makes reinjection important for sustained productivity. A dominantly ESE-WNW to nearly E-W extensional direction is confirmed by recent focal mechanism studies (Unruh et al., 2002). However, this extension is interpreted in the context of distributed dextral shear involving important fault zones of truly SE-NW orientation (op. cit.), some subsidiaries of which are drawn in Figure 1.

MAGNETOTELLURIC DATA ACQUISITION

The magnetotelluric data acquisition was contracted to Quantec Geoscience Inc., and basics of the MT method are summarized by Vozoff (1991). A simplified cartoon of an MT site deployment as used at Coso is shown in Figure 2. The electric (E) and magnetic (H) field components of the EM waves are measured with two types of sensors. The E field is a voltage difference taken over an L-array bipole span of nominally 100 m, divided by bipole length. Contacting endpoints of the bipoles were cold-rolled steel plates in holes ~20 cm deep with ~1 liter water added to improve contact. The H fields are obtained using high-sensitivity solenoids (coils) with built in preamplifiers, manufactured by EMI Inc. These are buried a similar depth for thermal and mechanical stability. Due to the remote nature of the sources and the high index of refraction of the earth relative to the air, the source fields are assumed to be planar and to propagate vertically downward. However two axes of E and three axes of H are measured because the scattering of EM waves by subsurface structure can be arbitrary in polarization, necessitating a tensor description.

Broadband EM times series are recorded by these devices, and they are decomposed into individual frequency spectra through Fourier transformation. Through band averaging and ratios, we arrive at the fundamental MT quantity which is interpreted for geological structure, the tensor impedance of the earth to vertically incident, planar electromagnetic wave propagation. This is expressed as:

$$\mathbf{E} = [\boldsymbol{Z}]\mathbf{H}\ ,$$

where $\boldsymbol{Z}$ is a two-rank tensor. Individual elements of the impedance are subject to simple arithmetic to obtain an apparent resistivity (ρ) and impedance phase (ϕ), which are more intuitive to inspect and interpret (Vozoff, 1991). The nominal frequency range recorded was from 250 Hz to 0.01 Hz, which spans a depth range of several 10's of meters to depths greater than 10 km. The assumption of a planar geometry to the MT fields is crucial in the interpretation of the data and artificial EM sources nearby can invalidate it. An obvious source could be the high voltage 60 Hz production of the field, which may be so strong under transmission lines or next to generation plants as to saturate MT recording electronics. Strictly speaking, however, the loss of a very narrow band of results around 60 Hz is generally not serious since the impedances are a smoothly varying function of frequency. More problematic are broadband noises whose causes are often obscure but can include power system load fluctuations (either within the Coso field or from nearby interstate transmission lines), rotating machinery, and vibration. These are especially onerous in the so-called MT "deadband", a frequency band spanning 3 - 0.1 Hz, where the MT fields are particularly weak and would correspond to depths ranging from 2 to 5 km in the reservoir that could be tapped for geothermal resources though deep drilling.

An example of MT time series taken at the Coso area ~0.5 km west of the Navy II power plant is presented in Figure 3. These are compared to series acquired simultaneously just east of Socorro, NM, some 600 miles to the east of Coso. Most obvious in the first portion of the plot at the Coso site is sinusoidal variation with a frequency of ~6 Hz which is absent at Socorro. The cause of this fluctuation is unknown. In the quieter portion of the plot, higher energy bursts of MT signal are seen at both sites (e.g., time 4:06:14 and 4:06:22; note that amplitude range of plots differs). However, the signal burst at 4:06:05 at Socorro is swamped by the noise source at Coso at the same time. During weaker signal times even with noise sources less obvious, the visible correlations between the two sites is often obscure, evidence of broad band noise of a lower level but still competitive with the signal. Note that the vertical magnetic field is completely dependent on lateral variations in resistivity structure, so that visible correlations even without noise are naturally more obscure.

"Local" Remote Reference Processing Attempts

The remote reference method (Vozoff, 1991) is designed to overcome environmental noise through coherent detection utilizing simultaneous, remotely recording sensors completely outside the influence of the noise sources. The reference site of course may have its own noises but as long as these are uncorrelated with the local site then the detection principle remains valid. Of course, the remote site should be of high fidelity or the final result will be degraded or a greater length of averaging time will be needed to achieve equivalent results (e.g., Egbert, 1997).

In the first Coso data campaign of 2003, reference sites were attempted at five locations of varying distance from the geothermal field (Wannamaker et al., 2004) (Figure 4). The nearer three sites which measured fields using the same equipment of the MT survey contractor include the Centennial Flat area approximately 15 miles north of the Coso field, Panamint Valley about 30 miles distant, and Amargosa Valley NV about 60 miles distant. Time series from these sites were downloaded to field PC by the local Coso collection crew for processing at essentially the same time as those in the Coso geothermal field, which is normal survey procedure. For the more distant references we discuss later, more elaborate communications procedures were required. An increasingly great distance for the reference was recognized as the survey proceeded, as we explain next.

The MT apparent resistivities corresponding to impedance elements Zxy and Zyx for the reference site at Centennial Flat and in Panamint Valley are shown in Figure 5. Characteristic of non-MT artificial effects are apparent resistivities which rise with decreasing frequency at an anomalously steep rate in the weak MT middle band, and then fall almost discontinuously around 0.1 Hz where the MT fields become quite strong again due to solar wind energy. This is apparent at the Centennial Flat site, as is the case for soundings generally in the Coso area processed using these nearer references. The effect is analogous to that seen in controlled-source (CSAMT) surveys when the transmitter is to close to the survey area (Zonge and Hughes, 1991; Wannamaker, 1997).

The distortion propagates to frequencies higher than 0.1 Hz to an unknown degree so that structural images in the pertinent depth range of several km may be unreliable. Essentially only the xy component is effected in the Coso survey, which corresponds to an E-field directed N-S (x-direction). This behavior implicates the Bonneville Power Authority (BPA) DC intertie, which runs in this direction nearby to the east of the Coso field (Figure 4), and which broadcasts electric fields roughly parallel to itself. Similar broadband non-plane wave effects due to interstate DC interties have been observed occasionally in other surveys (e.g., Wannamaker et al., 1997; 2002).

In an attempt to escape the influence of the DC intertie, remote references were tried also in Panamint Valley and Amargosa Valley, about 30 and 65 miles distant from the intertie respectively. The sounding from Panamint is shown in Figure 5 also. This good-quality sounding does not show the cusp-like behavior near 0.1 Hz seen in Centennial Flat, and the site at Amargosa Valley was even cleaner. Initially, we concluded from this that influence of the DC intertie at these distances was minimal and that the sites

references still showed significant cusp-like behavior in this frequency range (Figure 6, site taken ~1/2 km east of well 34-9), although the results using the more distant Amargosa site were better. This was disappointing as 65 miles of often winding road was reaching the limit in terms of practical, on-site reference retrieval.

It is evident that a site giving good quality plane-wave (MT) results does not necessarily serve as a good remote reference for soundings taken in a noisy environment. Clearly, EM fields which are correlated with the DC intertie are persisting at least as far away as the Amargosa Valley reference. This is occurring even though such fields have become planar by this point and only serve to improve the local MT responses at Panamint and Amargosa Valleys (e.g., Figure 5). The powerline fields in the Coso field area, which are quite non-planar, remain correlated in time with the Panamint and Amargosa sites and thus are not removed by remote reference processing. As emphasized by Wannamaker et al. (2004), a reference must be established which is completely outside the domain of the noise source in a survey, not just put

Distant Remote References: Parkfield California Observatory and Socorro New Mexico

More than 40 MT soundings had been taken at Coso using the various references just described before the far-reaching nature of the noise source was truly recognized. To obtain high quality results at these locations, we were faced with a complete reoccupation using a yet more distant reference (expensive), or else locate a reference site of opportunity which fortuitously happened to be running while the Coso survey was underway. Such a reference site in fact exists in the way of the Parkfield, CA, permanent MT observatory, run by the University of California at Berkeley seismic network (for info, see *http://quake.geo.berkeley.edu/bdsn/em.overview.html*) (PKD in Figure 4). Due to power law falloff and inductive dissipation of EM fields from a line-source, the DC intertie fields at PKD should be weaker than those at Amargosa by about a factor of 5, making the attempt to use PKD worthwhile. The EM time series are available at no charge essentially in real time through an ftp request. They are sampled at a rate which allows their use as a reference for frequencies up to 14 Hz, which covers the contaminated band at Coso. The contractor, Quantec Geoscience, Inc., successfully unwrapped the native SEED format of the time series and automated their use as references in their processing software. A plot of the results for site E13 appears in Figure 7 and indicates that the near-field effect has been corrected. The principal frequency range of distinction between the Parkfield-processed and the previous results is 1-0.1 Hz. Similarly good results were obtained for reprocessing the other ~40 sites of the Coso area.

This outcome is very fortunate, but there was concern that Parkfield is barely adequate in distance and that during times of exceptionally low natural MT field activity or large powerline fluctuations there still could be some soundings whose quality would be compromised. Hence, for the remaining MT sites at Coso taken by Quantec, a remote reference was set up near Socorro, NM (SOC), more than 600 miles to the east of the Coso field. Because it is important to recognize surveying problems as they may occur, the Coso and the reference time series should be brought together as quickly as possible. To achieve this, crew at Coso uploaded acquired time series to the University of Utah/EGI ftp site using the Caithness Energy high-speed computer facilities at Coso Junction. The contractor's data processor/reference operator in Socorro downloaded these series from Utah using the high-speed computer facilities of the New Mexico Institute of Mining and Technology. Coso site and reference time series thereby were combined several hours after their acquisition.

To verify that the MT time series at Socorro are well correlated with those at Coso, and Parkfield, we show in Figure 8 a 2 min segment taken simultaneously from site E29, PKD and SOC. This is an unusually quiet segment of time at E29 and excellent correlations are seen both between the impulsive, high-frequency data due to regional-scale lightning energy, and the low-frequency magnetospheric signals, at all three sites. Site E13 was not reoccupied during the second deployment using the Socorro reference, but we can compare results from site E29 processed with PKD with those processed using SOC (Figure 9). The sounding curves are essentially identical indicating that Parkfield was an adequate reference in this case, although we view Socorro with more assurance as a quiet site outside the influence of the DC intertie. The unusual effort required to establish a quiet remote reference free from both local and broadscale artificial EM interference has been completely necessary. The zones of producing fractures at Coso reside in the 1-3 km depth range (Adams et al., 2000) in plutonic rocks mantled by a variable layer of altered overburden. This situation determines the first order character of the soundings shown thus far, namely apparent resistivities in the 10-30 ohm-m range for frequencies higher than 3-10 Hz rising to values near 100 ohm-m at lower frequencies. Subtle variations in the upward slope of the apparent resistivity, and corresponding impedance phase responses provide the second-order evidence for bedrock structure of potential geothermal significance. Thus, high quality MT soundings are required.

Unfortunately in the second data campaign of 2005, the contractor (Apollo/Phoenix Geophysics) did not implement such a distant remote reference and the data were contaminated similarly as in our first campaign before action was taken to use distant remote reference sites (Parkfield and Socorro). Nevertheless these data were judged to be of sufficient accuracy down to 0.1 Hz that they could be included in a 3D MT interpretation of the Coso field site. Because these data are not as accurate as the processed data acquired in the first phase of the measurements, we cannot expect to extract subtle variations in the data to the same degree as with the data acquired in 2003. Nevertheless they are useful in constraining the southern boundary of the geothermal field.

MAGNETOTELLURIC INVERSION

Our ultimate aim is to construct a 3D conductivity model of the Coso geothermal system and use it to better understand the hydrothermal system by correlating it with independent geological and other geophysical information. To accomplish this we apply an inversion process, where the observed impedance data are fit in a least squares sense to model data. The model data are produced by solving Maxwell's equations for 3D conductivity variations and plane wave source excitation at a discrete set of frequencies. These frequencies correspond to those used to specify the impedance tensor in the field measurements. To stabilize the inversion process, additional constraints are added such as spatial smoothing and bounds on the conductivity model. Because the resources for 3D MT inversion and modeling are highly demanding, requiring significant computational resources and time (Newman and Alumbaugh, 2000; Newman et al., 2003), it is more efficient to start to build the 3D conductivity model from 2D imaged sections of the reservoir. This starting model will be refined subsequently through the 3D inversion process.

2D Data Interpretation

The initial 2D inversion was performed on relatively sparse east-west profiles of 8-10 MT sites selected from the survey map in Figure 10, utilizing the 2D MT inversion algorithm of Rodi and Mackie (2001); we did not use the 2005 data in this exercise because of noise problems below 0.1 Hz due to the lack of a good remote reference. The inversions were carried out using Z_{yx} impedance data and analyzed assuming the electric field is polarized perpendicular to a presumed N-S geological strike (x-axis); in actuality, polar diagrams show that geological strike varies with frequency and so is 3D, but at the lowest frequencies (<0.1 Hz), the polarization ellipses align in a north-northeast direction, which follows the trend of the Basin and Range fault-block geology. In spite of the obvious limitations in modeling and inverting the Coso data in 2D, it is a logical starting point for carrying out a full 3D analysis of the data. The Z_{yx} apparent resistivity and phase are defined as the transverse magnetic (TM) mode for use in the 2D inversion here because 3D modeling shows that it is usually more robust than the TE data to non-2D effects such as finite strike and static shifts (e.g., Wannamaker et al., 1984; Wannamaker, 1999).

Shown in Figures 11 and 12 are 2D fits to Coso data (ρ and ϕ) along the profile containing MT station locations 45 through 53. Fits to the apparent resistivity data (red curves) agree closely with the field observations over the entire frequency band. The phase data, however, are not fit as well, especially below 0.1 Hz, most likely indicating a three-dimensional characteristic of the data. The resulting 2D resistivity depth section for this profile, as well as those from other profiles, are presented in Figure 13. Perhaps the most conspicuous feature of our ensemble of 2D inversion sections is a moderate low resistivity zone dipping steeply west from the Coso east flank area; between 79,000 and 77,000 Northing. This zone terminates abruptly both to the south and the north. Several of the more productive wells on the east flank dip toward this structure suggesting some correlation with higher permeability and fluid content. Wannamaker (2004) first identified this conspicuous feature using 2D TM mode analysis of the dense array line NA1 shown on Figure 10. The 2D inversion model of this line (Figure 14) provides more detail than individual sections of the 3D conductivity model due to the contiguous sampling over 52 bipoles, each 100 m in length. The NA1 line inversion also shows the west dipping lower resistivity zone seen in the sections of Figure 13. Producing well 34-9RD2 grazes this zone along its east boundary. Over the bottom ~35 m of well 34-9RD2, where it approaches the conductor most closely, was encountered an enormous lost circulation zone representing substantial open porosity (P. Rose, 2006, pers. comm.). Shallow low resistivity material in the model represents thin alluvium and clay alteration over the east flank, plus deeper alluvium of Coso Wash toward the east part of the model section. Wannamaker (2004) noted that it was necessary to consider a 3D interpretational framework to fully explain both TM and TE modes of data.

3D Inversion of the Coso Field Data

The massively parallel algorithm described by Newman and Alumbaugh (2000) was used for the 3D modeling and inversion of the Coso field data, where eight 2D TM mode inversions shown in Figure 13 were spatially interpolated to form the core of a 3D model beneath the data acquisition sites. This core model was then extended laterally over 100 km and to nearly 100 km in depth. The large area around the core model is required to satisfy the boundary conditions (scattered fields are assumed to be zero on the boundary) of the finite-difference model. The resulting 3D finite difference (FD) grid used to simulate data arising from the model, employed 244 by 258 by 120 nodes in the X, Y and Z directions respectively. The FD cells were 100m cubes within the central portion of the mesh defined by the data acquisition sites.

Away from the site locations the mesh cells grew to the outer boundaries. A maximum aspect ratio on cell dimensions was 8 to 1, so that no dimension of a boundary cell was greater than 800m. The interpolated 3D conductivity model provided the starting model for the 3D inversion. The simulated fields (Z_{xy} and Z_{yx} apparent resistivity and phase) for this starting model are shown in Figures 15 and 16 and are compared with the corresponding field observations for sites 45 through 53.

For frequencies above 1 Hz, the 3D fields generally show good correspondence with the field data for both polarizations, even though there are some grid-induced statics arising from the interpolation process that affect primarily the predicted Z_{xy} apparent resistivity at a few sites. It is expected that the Z_{yx} data would be the least well fit by the 3D model because it is constructed of 2D sections generated by fitting the Z_{yx} data. Significant differences, however, arise at all sites between the model and field curves in both apparent resistivity and phase at lower frequencies. When the field data were analyzed using 2D assumptions, such discrepancies were most apparent in the phase data.

While all the complex impedance tensor elements can be considered as data in the inversion, it was found that the on-diagonal terms (Z_{xx}, Z_{yy}), which have much lower magnitude, and thus lower signal-to-noise, than the off-diagonal terms (Z_{xy}, Z_{yx}), generally degraded the performance of the inversion. Thus we included only the off-diagonal elements. Also designing a FD mesh that will accurately represent the electromagnetic fields over the entire range in the inversion of the observed data can be quite challenging. Practical considerations required that the entire frequency range of the data was not fit simultaneously at first, but in three phases. In the solutions presented here we first restricted the 2003 data over the frequency range 250 to 1 Hz utilizing a mesh 120 nodes along each coordinate direction that spanned distances of 120 km in the horizontal dimensions to satisfy boundary conditions. This mesh also extended 30 km into the air and 60 km into the Earth. The smaller mesh for this frequency band (250 to 1 Hz) allowed for fast processing times and the model obtained was used as a starting model in the next phase of the image processing. In the second phase we added 2003 data down to 0.3 Hz and in the final and third phase we added the data acquired in the 2005 campaign (250 to 0.3 Hz). To accommodate the lower frequency data in phase two and three of the image processing, we expanded the mesh to 244, 258 and 120 nodes to move its boundaries out a sufficient distant to insure quality results. The accuracy of these two meshes were tested and verified to within a few percent based on 1D forward models over the two frequency ranges, and were shown to have depth sensitivity to 5 and 15 km respectively. This should be adequate for mapping the depths of interest in the geothermal system.

Out of the 102 MT stations acquired in 2003 over the East flank of the Coso Field, only one station was discarded because of severe noise problems. We discarded six stations from the 2005 measurements. In the inversion processing we assumed a 5 percent noise floor, based upon the amplitude of each impedance measurement, where the data were weighted by the noise estimates. The first 3D inversion analysis (250 to 1 Hz data) was carried out at the National Energy Research Scientific Computing Center (NERSC), where 512 IBM SP2 processors were employed. On this platform for a 48-hour period, 15 inversion iterations could be completed on average. Shown in Figure 17, is a plot of the convergence of the inversion iteration. The dashed curve is a plot of the convergence of the error functional with regularization constraint. The step-like features in this plot correspond to reducing the level of smoothing in the inversion process as the iteration proceeded. The solid curve is a plot of the weighted squared error, the data misfit without regularization. While we have yet to achieve the target data misfit of one, we observed a good reduction in the weighted squared error from 149 to 4.8 at the 88th inversion iteration. Subsequent analysis using the lower frequency data was carried out on a more powerful Infiniband Linux cluster utilizing 100 processors; for the same number of processors the Linux cluster is about 3 to 5 times faster than the NERSC platform. With the 2003 augmented data we were able to reduce the data misfit to 2.99, which is still a factor of three above the desired noise threshold. However when we add the 2005 data the final misfit we could achieve was 3.2. Closer inspection of the data fits indicates the inability to fit the data to the assumed noise threshold appears to arise from noise in the MT deadband, 3 to 0.3 Hz, which also appears to affect the 2005 data more so than the 2003 data; this should come as no surprise given the use of a "local" remote reference in the 2005 survey. Nevertheless the predicted data produced from the conductivity model based on both the 2003 and 2005 data sets showed good improvement with the field data compared with the predicted data produced from the starting model (Figure 18).

The 3D Conductivity Model

The 3D conductivity model produced from the inversion of the 2003 and 2005 survey data is illustrated in Figure 19. The most obvious feature is the red core of high conductivity centered within well production and reinjection intervals along with micro-earthquake locations. These locations appear to correlate with transition boundaries in the conductivity to some degree; we will have more to say about this later. The model was further refined using the both 2003 and 2005 data (250 to 0.1 Hz) in the 3D imaging algorithm. A horizontal depth slice from the final model at 500 m above sea-level (~700 m below ground surface) is shown in Figure 20. The mapped surface location of faulting is shown as green lines, along with the locations of vertical sections of this model shown in subsequent figures. The two most prominent features of the conductivity structure at this depth are; 1) the high conductivity in the central portion of the figure that persists from the prior models and 2) the correlation between the high resistivity / low conductivity band and the series of right-lateral faults running south to north in the center of the figure. The high conductivity region is bounded to the north-east and south-west by the mapped surface expression of faults, implying the faulting is nearly vertical to depths of 1,000 m below the surface.

Figure 21 shows a vertical (west to east) section at Northing 81,000 m. The locations of the Coso Wash Fault (indicated by (1)) and two other un-named faults are shown. In the eastern half of the section the structure clearly dips to the east. The conductivity structure implies that the Coso Wash graben sediments are no deeper than ~1,000 m in this vicinity. The two unnamed faults to the east (marked 2 and 3) correlate with the easterly dipping conductivity structure and sediment thicknesses increasing to depth of ~2,000 m below ground surface. To the west the conductivity structures show nearly vertical contacts between low and high conductivity material. Figure 22 shows a vertical (west to east) section at Northing 79,900 m that intersects the Coso Hot Springs. The hot springs are located directly above a high resistivity feature on the easterly dipping contact between the central resistor and the more conductive valley fill to the east.

The location of the high density MT line of Wannamaker (2004) is shown in Figure 20 corresponding to the 2D resistivity section shown in Figure 14. The vertical section through the 3D model at the location of the 2D line as well as a section 700m to the south is shown in Figure 23 for comparison. The 2D and 3D inversion sections to first order imply that the dipping conductor becomes much more pronounced southward from the dense array line. The 3D inversion sections overall are expected to be a more accurate representation of structure directly beneath them because an attempt is made to fit both TM and TE modes of all profiles simultaneously. However, we do not believe the conductor imaged under the dense array line is entirely due to sideswipe from higher conductivity 500 m or more to the south because the 2D image in Figure 14 where it comes near the surface is only 200-300 m wide. We conclude there must be a vestige of the dipping conductor under or very close to the array line, but the advantage of 3D coverage is that the maximal expression of the conductor can be pinpointed with more confidence.

A north-south transect that intersects the Devil's Kitchen structure is shown in Figure 24. As with the conductivity structure beneath the Coso Hot Springs, Devil's Kitchen is located over a high resistivity feature at depth. The location of Devil's Kitchen also coincides with the surface termination of a conductivity-resistivity contact that would suggest a fault that in Figure 24 dips to the north from Devils' Kitchen. The southerly portion of depth section shown in Figure 24 intersects an area of high geothermal well density, where the highly conductive near surface is interpreted as a clay cap alteration zone manifested from the geothermal fluids and chemistry beneath. The producing intervals of all the wells between 717,400 and 717,900 m Easting are shown as nearly vertical black lines. A single injection interval is shown as a red vertical line. This figure illustrates two general observations about the correlation between well production intervals and the conductivity structure; 1) to the north of Northing 76,000 the producing intervals are located in or near the transition zone between low and high conductivity, 2) in the south-west area of our survey (south of Northing 76,000) lies an area of intermediate conductivity (~0.02 S/m) with no sharp contrasts in conductivity where many successful production intervals lie. The first observation suggests that the deformation caused by the emplacement of younger material into existing rocks has produced significant fracturing on the boundaries (represented by the transitions between low and high conductivity). The fracturing at the boundaries provides good permeability for geothermal fluid production. We will discuss the significance of the correlation between well production and the non-descript conductivity zone in the south-west of the survey when we come to consider the correlations with the seismic velocity model for the area.

The geophysical signature

Electrical conductivity and seismic velocity depend on many physical conditions. Within the complexity of a geothermal system is it difficult to isolate unique relationships that allow an unambiguous interpretation of inferred geophysical parameters such as electrical conductivity, acoustic and shear velocity. Just as the physical properties, mineral composition, fracturing, fluid saturation, temperature, porosity and pressure, affect the geothermal characteristics of the subsurface, they also affect the geophysical parameters that can be inferred from the surface. In this study we raise first order correlations between seismic and electrical geophysical structure and suggest causative mechanisms for anomalous regions.

Electrical conductivity is primarily a function of water saturation, porosity and the electrical conductivity of the water filling the pore space (Palacky, 1987). In fractured media, porosity is dominated by fracture porosity. The electrical conductivity of the pore water is controlled to first order by salinity and to second order by temperature. The mineral composition of the rock matrix and clay content of the porosity (inter-granular in the case of sedimentary rocks and fractures in the case of igneous and metamorphic rocks) also has a first order effect on the bulk electrical conductivity of rock.

For rock of relatively uniform composition both acoustic and shear velocity decreases with increasing temperature (Christensen, 1989). Acoustic velocity generally decreases faster than shear velocity resulting in a decrease in the V_p/V_s ratio as temperature increases. Rock with randomly oriented fractures show decreased V_p and V_s compared to un-fractured rock. The V_p decreases less than V_s as the density of fractures increases resulting in a general increase in V_p/V_s as fracture density increases (Schön, 1996). Acoustic velocity generally increases as fluid saturation increases while the shear velocity remains only slightly effected (through the change in density).

The MT conductivity model, the MEQ velocity model and interpretation

A synthesis of much of the previous geochemical and geophysical work at Coso is presented by Lees and Wu (2000). They present an intrusive model for Coso that places a magmatic body at depths greater than 5 km below the triangle formed by MEQ stations S1-S3-S4. MEQ stations S1 and S4 are shown in Figures 20 and 25, with S3 located approximately 3 km to the west of S1. Lees and Wu (2000) propose the following model. The center of magma movement is close to the S1-S3-S4 triangle (just to the south-west of our MT survey). Hot magma arose from depth and spread out in all directions. It flowed due north and due east following the two pre-existing sets of faults. Northeast of the spreading center, there is a strong, unfractured rock body which is the high velocity, less porous, fluid-depleted region.

The 3D velocity model derived from tomographic inversion of micro earthquake (MEQ) data (Wu and Lees (1999) and Lees and Wu (2000)) was provided to us for comparison with the 3D MT conductivity model. The tomographic model used a cell size of 200 m by 500m in the horizontal and vertical directions respectively. The MEQ inversions produce models of acoustic (V_p), shear (V_s) velocity and the associated V_p/V_s ratio.

Examination of the 3D velocity model shows many interesting correlations (and non-correlations) with the 3D conductivity model. Figure 25 shows a horizontal slice through V_p/V_s at 500 m above sea-level with the same surface features and markers used in Figure 20. The correlation between the high V_p/V_s and high conductivity in the central portion (between 718,500 and 720,500 Easting and 76,500 and 78,500 Northing) of the section is striking. To the north the low V_p/Vs and low conductivity both align with the surface expression of the Coso Wash Fault. An area of interesting difference lies in the south-west corner of the plan section, where the conductivity model shows intermediate conductivities, on the order of 0.02 S/m, with no discernable structure whereas there is a distinct ring shaped structure of high V_p/V_s ratio.

Figure 26 shows a 3D perspective view of the combined MT conductivity and MEQ velocity models. The vertical sections are of log10 conductivity while the horizontal slice (500 m above sea level) is of the V_p/V_s ratio. The V_p/V_s ring structure along with geothermal well production intervals is seen in the south-west corner of the figure.

The south-west corner of the MT survey (MT stations 78, 87, 88, 96, 99 and 100) is the area with the anomalous ring structure seen in the V_p/V_s ratio (Figure 25) with only slightly decreased electrical conductivity (Figure 20). This area has significant geothermal production from depths of 2-3 km. Whereas the V_p/V_s ratio map provides a clear indication of production intervals in the south-west portion of the survey area, the electrical conductivity does not. This lack of correlation between the V_p/V_s and conductivity structure in this region may be attributed to the truncation of the MT survey data. We suggest that better correlations could be obtained if the MT data can be acquired to the south and west.

Toward the north-east is a north-west to south-east trending band of low electrical conductivity and low V_p/V_s ratio to the north-east of which is the large high V_p/V_s and electrical conductivity region (between 718,500 and 720,500 Easting and 76,500 and 78,500 Northing) bounded by two sets of mapped faults. This area of low V_p and V_s, and of high V_p/V_s, is interpreted by Lees and Wu (2000) as probably fluid-saturated. While this is consistent with high electrical conductivity, an alternate possibility exists, as described below. To the north and east of Devil's Kitchen is a south-west to north-east trending zone of low V_p/V_s and electrical conductivity and generally aligns with the surface expression of the Coso Wash Fault. This feature is seen in the center of Figure 22 with nearly vertical boundaries between low and high conductivity to the west and an easterly dipping contact to the east. These areas are interpreted as relatively unfractured, unsaturated less permeable rock.

There is a distinct difference between the area in the south-west of Figures 20 and 25 where high V_p/V_s correlates with moderate electrical conductivity (~0.02 S/m) and the area to the north-east (MT stations 63, 64,72, 82, 81, 70, 63) where high V_p/V_s correlates with high electrical conductivity (~1.3 S/m). Recent wells drilled on the eastern flank of this latter structure into the transition zone between low and high conductivity encountered large open fractures that caused high rates of mud loss (Figure 27) (F. Monastero, pers. comm., 2005) indicating that fluids there were underpressured at best. The fact that large open fractures were encountered along the flanks of the high conductivity plus the high V_p/V_s feature suggests that this is an area that is highly fractured and that fluids are nearby. Temperatures at depth appear too high to support conductive smectite clays (>200 C for depths below 2.5 km).

Conclusions and Plans

High quality broadband MT data can be acquired in the Coso geothermal field following efforts to establish an adequately distant, clean remote reference. It is not sufficient to use a reference site which appears to give good plane-wave results local to the reference. This is because there may be EM noise fields (albeit planar) at the reference site that are correlated in time with those of the survey area, which are non-planar in geometry. In the 2003 survey, we found that MT time series at the permanent Parkfield observatory in California were adequate as reference fields to the sites at Coso. In the course of doing this, technology has been established by the contractor to utilize the Parkfield fields in MT surveying generally, thereby improving survey quality for other applications. Noise sources of scales as broad as that of the BPA DC intertie are rare, but this particular one may be a factor in exploration of numerous other geothermal systems in western Nevada and easternmost California due to its proximity.

A 3D conductivity model of the Coso geothermal field has been constructed using full 3D inversion of 124 MT sites over a frequency band of 250 to 0.3 Hz. In order to produce a geologically meaningful results the starting model was constructed from a series of 2D resistivity images along east-west transects, approximately perpendicular to the regional geological strike. The 2D inversions were carried out using Z_{yx} impedance data and analyzed assuming the electric field is polarized perpendicular to a presumed N-S geological strike. We employed this strategy to save time and because model equivalence continues to be a serious issue in the interpretation of MT data, especially in three-dimensions. Without recourse to a good starting model, a 3D imaging experiment may not provide the value added information. Many factors determine the quality of an image, including not only the starting model, but the type of noise in the data, its frequency band employed, spatial coverage and the robustness of the imaging algorithm.

No doubt 3D MT imaging will be an ongoing research topic for years to come. From the Coso experiment, we conclude that removal of statics was very effective within the 3D inversion process, but activation of the deeper parts of the model space, below 1 km depth proved difficult without recourse to a good starting model. We believe there are ways to remedy this shortcoming by incorporating lower frequency data within the inversion process at the expense of larger grids and greater computational costs. Use of more effective depth weighting schemes and preconditioning the inversion iteration may also be helpful and we are now investigating. Nevertheless the focus of the current work is on an integrated MT interpretation of the Coso MT measurements and correlations with independent geophysical data sets and geological and well information. We believe the major correlations found thus far are convincing enough and provide a level of confidence in 3D conductivity model derived for the Coso system.

ACKNOWLEDGEMENTS

Data collection and processing were supported under U.S. Dept. of Energy contract DE-PS07-00ID1391 and Dept. of the Navy contract N68936-03-P-0303 to the Energy & Geoscience Institute. We thank Coso Operating Company for access to the field and to the high-speed internet services which made the ultra-distant remote referencing possible. Similarly we are grateful to New Mexico Institute of Mining and Technology (Prof. Harold Tobin) for providing a quiet reference site and fast ftp access. We also thank Frank Monastero and Allan Katzenstein of the U.S. Navy Geothermal program office for support and encouragement, and for funding all archeological site clearances. Finally, the competence and diligence of the field crew of Quantec Geoscience, principally Jon Powell, Joel Cross, Claudia Moraga, Bill Doerner and Ken Nurse, made results of this quality possible. Valuable discussions on MT data processing and use of the Parkfield facility were held with Gary Egbert. The data interpretation carried out at Lawrence Berkeley National Laboratory was supported with funding provided by the Department of Energy

Geothermal Program Office under Contract No. DE-AC02-05CH11231 with additional funding provided

REFERENCES

Adams, M. C., Moore, J. N., Bjornstad, S., Norman, D. I., 2000, Geologic History of the Coso Geothermal System, *Geothermal Resources Council Transactions,* **24**, 205-209.

Christensen, N. I., 1989, Seismic velocities, in *CRC Practical Handbook of Physical Properties of Rocks and Minerals*, edited by R. S. Carmichael, 1-228, CRC Press, Boca Raton, Fla.

de Lugao, P. P., and Wannamaker, P. E., 1996, Calculating the two-dimensional magnetotelluric Jacobian in finite elements using reciprocity: Geophys. J. Int., **127**, 806-810.

Egbert, G. D., 1997, Robust multiple station magnetotelluric data processing, *Geophysical Journal International*, **130**, 475-496.

the Coso Geothermal Field, *Proc. 28th Workshop on Geothermal Reservoir Engineering*, Stanford University, Stanford, CA, Jan. 27-29, SGP-TR-173.

Lees, J. M., and Wu H., 2000, Poisson's ratio and porosity at Coso geothermal area, California: J. Volc and Geothermal Res, **95**, 157-173.

Manley, C. R., and Bacon, C. R., 2000, Rhyolite thermobarometry and the shallowing of the magma reservoir, Coso Volcanic Field, California, *Journal of Petrology*, **41**, 149-174.

Newman, G. A. and Alumbaugh, D. L., 2000, Three-dimensional magnetotelluric inversion using non-linear conjugate gradients: Geophysical Journal International, **140**, 410-424.

Newman, G. A., Recher, S., Tezkan, B. and Neubauer, F. M., 2003, 3D inversion of a scalar radio magnetotelluric field data set: Geophysics, **68**, 791-802.

Palacky, G. J., 1987, Resistivity characteristics of geologic targets: in, Electromagnetic methods in applied geophysics, ed. by Nabighian, M. N., **1**, Soc. Explor. Geophys., Tulsa, 53-130.

Rodi, W. and Mackie, R. L., 2001, Nonlinear conjugate gradients algorithm for 2-D magnetotelluric inversion: Geophysics, **66**, 174-187.

Journal of Geophysical Research, **85**, 2434-2440

Schön J. H., 1996, Physical Properties of Ricks: Fundamentals and Principlrd of Petrophysics, **18**, Handbook of Geophysical Exploration, edited by K. Helbig and S. Treitel, Pergamon, Terrytown, N.Y.

Sheridan, J., Kovac, K., Rose, P., Barton, C., McCulloch, J., Berard, B., Moore, J., Petty, S., and Spielman, P., 2003, In situ stress, fracture and fluid flow analysis – east flank of the Coso geothermal system, *Proceedings 28th Workshop on Geotermal Reservoir Engineering*, Stanford University, Palo Alto, CA, Jan. 27-29, SGP-TR-173.

of the Coso Range-Indian Wells Valley region, California: transtensional deformation along the southeastern margin of the Sierran microplate, in Geologic evolution of the Mojave Desert and

Amer. Mem. **195**, 277-294.

by Nabighian, M. N., **2B**, Soc. Explor. Geophys., Tulsa, 641-711.

Geophysics, **62**, 451-476.

Wannamaker, P. E., 1999, Affordable magnetotellurics: interpretation in natural environments, in Three-dimensional electromagnetics, ed. by M. Oristaglio and B. Spies, Geophys. Devel. Ser., **no. 7**, Soc. Explor. Geophys., Tulsa, 349-374.

Wannamaker, P. E., 2004, Creation of an enhanced geothermal system through hydraulic and thermal stimulation – magnetotelluric surveying and monitoring: Quarterly Project Information and Planning (PIP) Report, July 1 – September 30, 2004, US Department of Wind and Geothermal Technologies, Enhanced Geothermal Systems Program, also see

Wannamaker, P. E., Hohmann, G. W., and Ward, S. H., 1984, Magnetotelluric responses of three-dimensional bodies in layered earths: Geophysics, **49**, 1517-1533.

Wannamaker, P. E., Stodt, J. A., and Rijo, L., 1987, A stable finite element solution for two-dimensional magnetotelluric modeling: Geophy. J. Roy. Astr. Soc., **88**, 277-296.

Wannamaker, P. E., J. M. Johnston, J. R. Booker and J. A. Stodt, 1997, Anatomy of the Southern Cordilleran Hingeline, Utah and Nevada, from deep resistivity profiling: Geophysics, **62**, 1069-1086.

Wannamaker, P. E., G. R. Jiracek, J. A. Stodt, T. G. Caldwell, A. D. Porter, V. M. Gonzalez, and J. D. McKnight, 2002, Fluid generation and movement beneath an active compressional orogen, the New Zealand Southern Alps, inferred from magnetotelluric (MT) data: J. Geophys. Res., **107(B6)**, ETG 6 1-22.

Wannamaker, P. E., Rose, P., Doerner, W., Berard, B., McCulloch, J. and Nurse, K., 2004, Magnetotelluric surveying and monitoring at the Coso geothermal area, California, in support of the enhanced geothermal systems concept: survey parameters and initial results: Proc. 29th Workshop on Geothermal Reservoir Engineering, Stanford University, Stanford California, January 26-28, SGP-TR-175.

Whitmarsh, R. S., 2002, Geological map of the Cactus Peak 7.5' quadrangle; Inyo County, California, CD-ROM map, in Geologic evolution of the Mojave Desert and Southwestern Basin and Range, ed. by Glazner, A. F., Walker, J. D., and Bartley, J. M., Geol. Soc. Amer. Mem. **195**.

Wu H., and Lees, J. M., 1999, Three-dimensional *P* and *S* wave velocity structures of the Coso Geothermal Area, California, from microseismic travel time data: J. Geophys. Res, 104, **B6**, 13,217-13,233.

Zonge, K. L., and Hughes, L. J., 1991, Controlled source audiomagnetotellurics, in Electromagnetic methods in applied geophysics, ed. by M. N. Nabighian, **2B**, Soc. Expl. Geophys., Tulsa, 713-809.

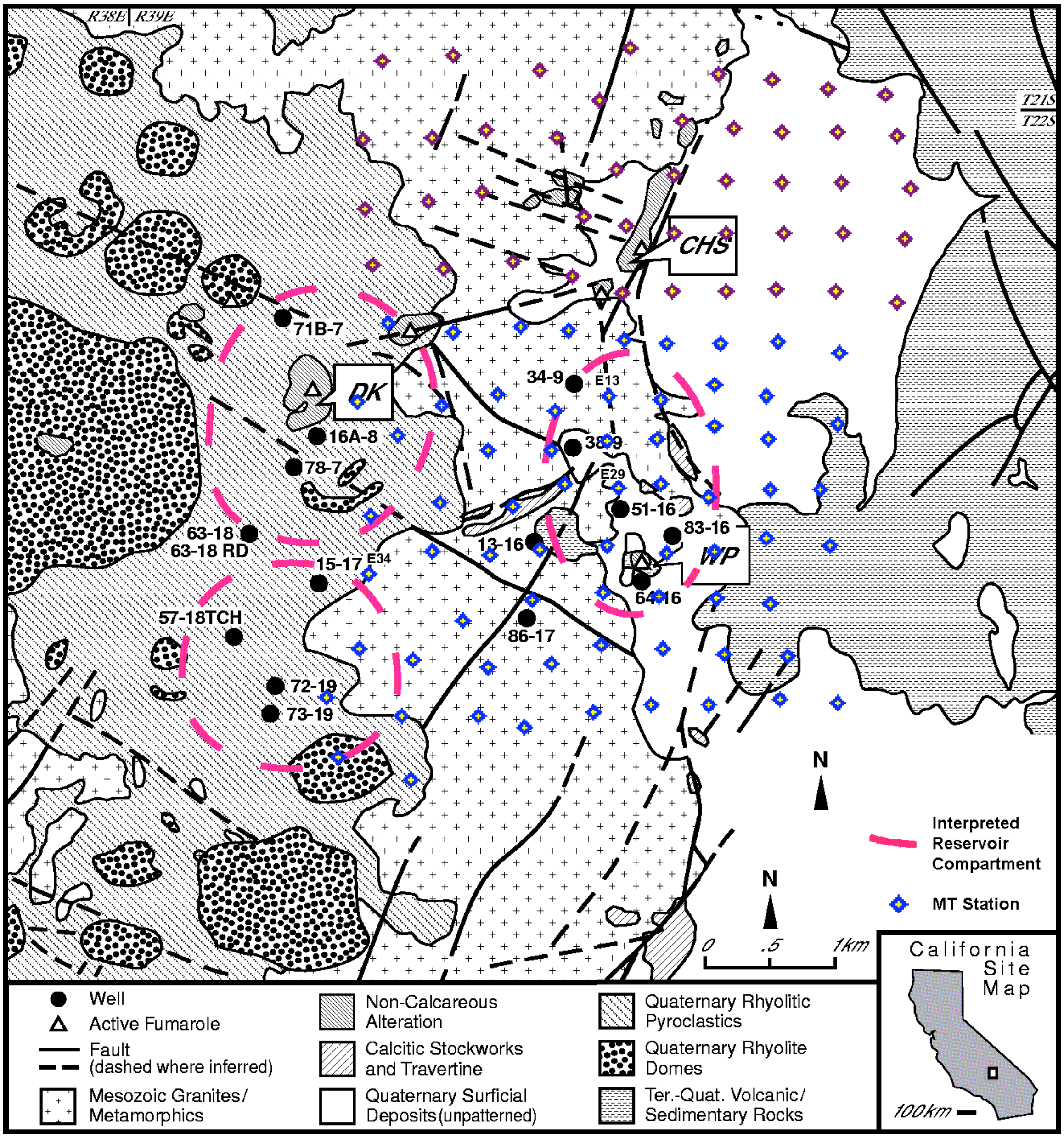

Figure 1. Simplified geological map of the Coso geothermal area including interpreted reservoir compartmentalization (after Adams et al., 2000), and MT data sites acquired in 2003. Geology map somewhat modified from Adams et al. (2000) based on Whitmarsh (2002). Principal alteration areas Devil's Kitchen (DK), Coso Hot Springs (CHS), and Wheeler Prospect (WP) are shown.

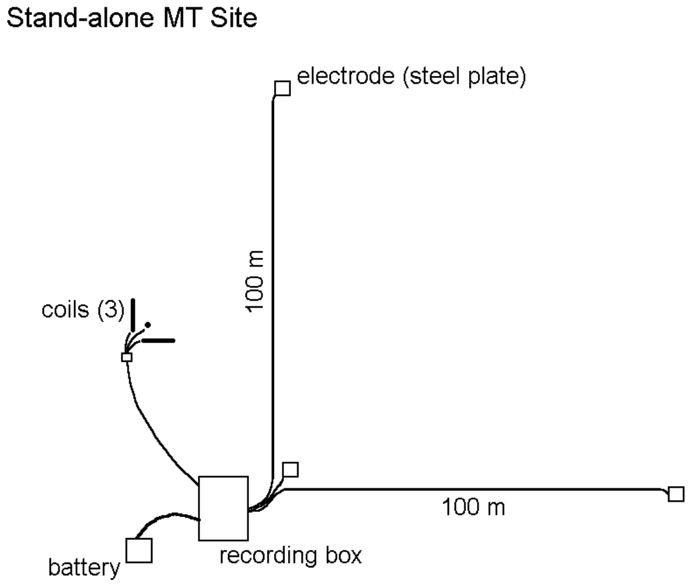

Figure 2. Simplified view of an MT station as deployed at the Coso geothermal field.

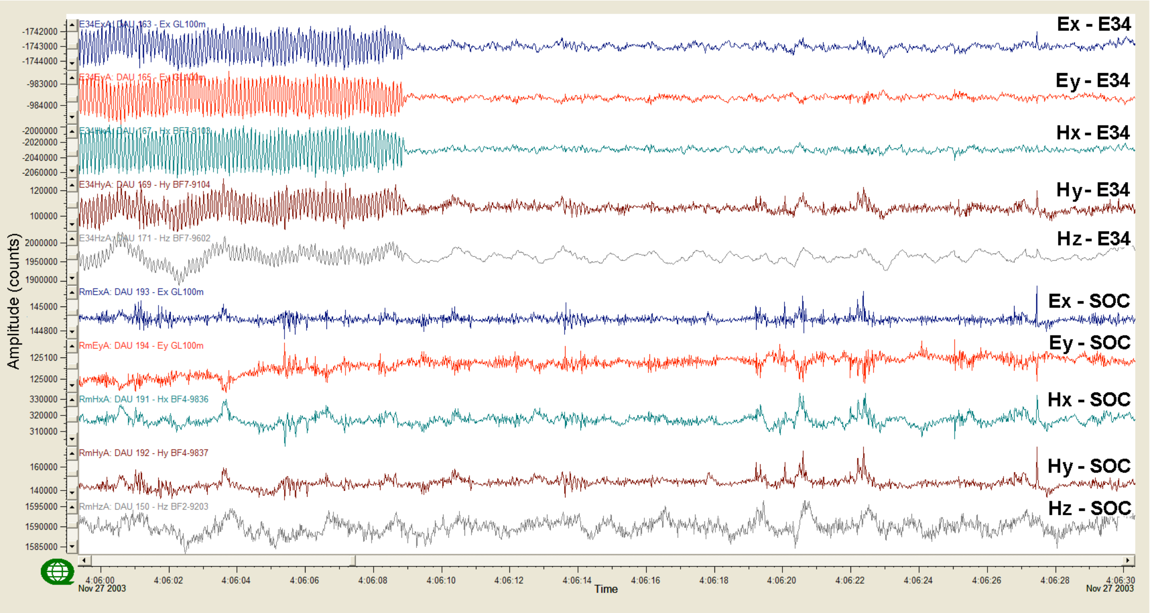

Figure 3. A 30 s segment of MT time series taken at site E34 (Figure 1) in the Coso field (top five traces)

to series taken near Socorro, NM. Ordinates are full scale plots, so relative amplitude factors may differ.

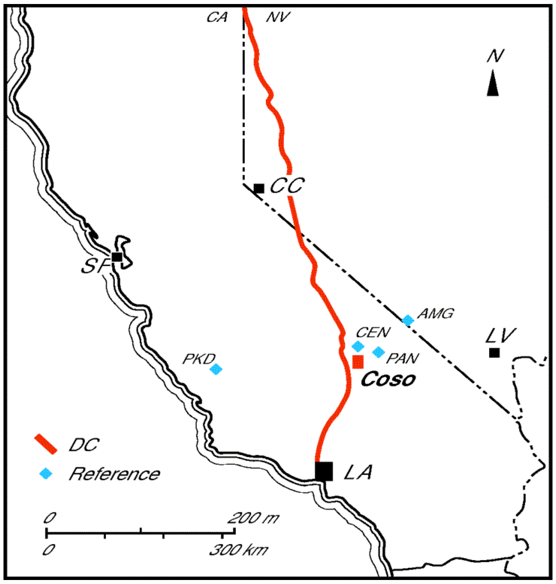

Figure 4. Locationof "remote" MT references in the vicinity of the Coso geothermal field. These are Centennial Flat (CEN), Panamint Valley (PAN), Amargosa Valley (AMG) and Parkfield (PKD). Not shown is Socorro, NM, some 600 miles to the east. Also shown is trace of BPA DC intertie line (red) which passes within a few miles of the Coso field. Urban centers include San Francisco (SF), Los Angeles (LA), Las Vegas (LV), and Carson City (CC). DC intertie trace provided by Jim Lovekin.

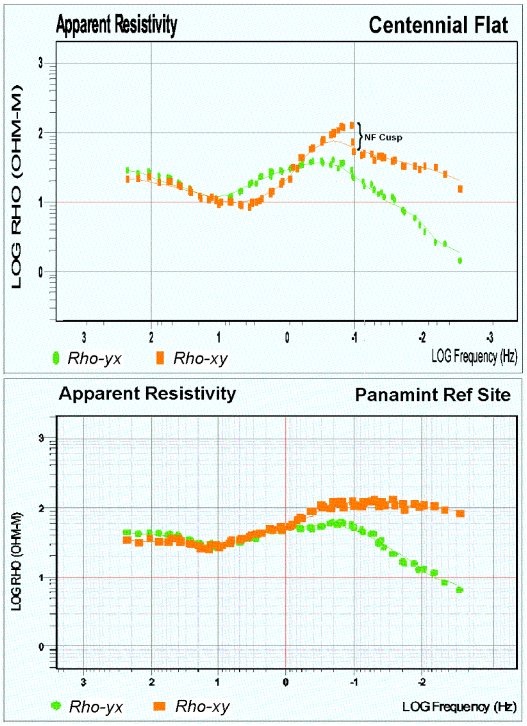

Figure 5. Apparent resistivity soundings taken at Centennial Flat about 15 miles north of Coso field, and in eastern Panamint Valley, about 30 miles northeast of the field. Note the abrupt change in Rho-xy around 0.1 Hz, indicative of a near-field (NF) or non-MT source field effect, in the former (closer) site, but its absence in the further site.These plots are as provided by the contractor before final processing and band-averaging to define inversion data.

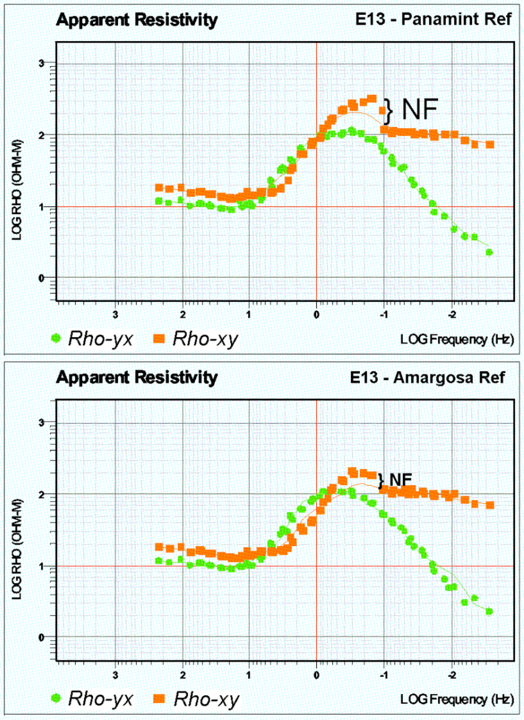

Figure 6. Apparent resistivity data from site E13 (Figure 1) in the Coso geothermal field processed using sensors in Panamint Valley (upper) and in Amargosa Valley (lower) as remote references. Some near-field effect appears to remain near 0.1 Hz

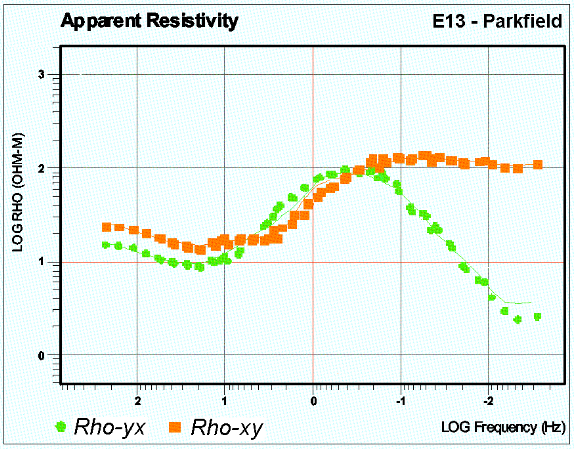

Figure 7. Apparent resistivity data from site E13 in the Coso geothermal field processed using the Parkfield MT observatory as a remote reference.

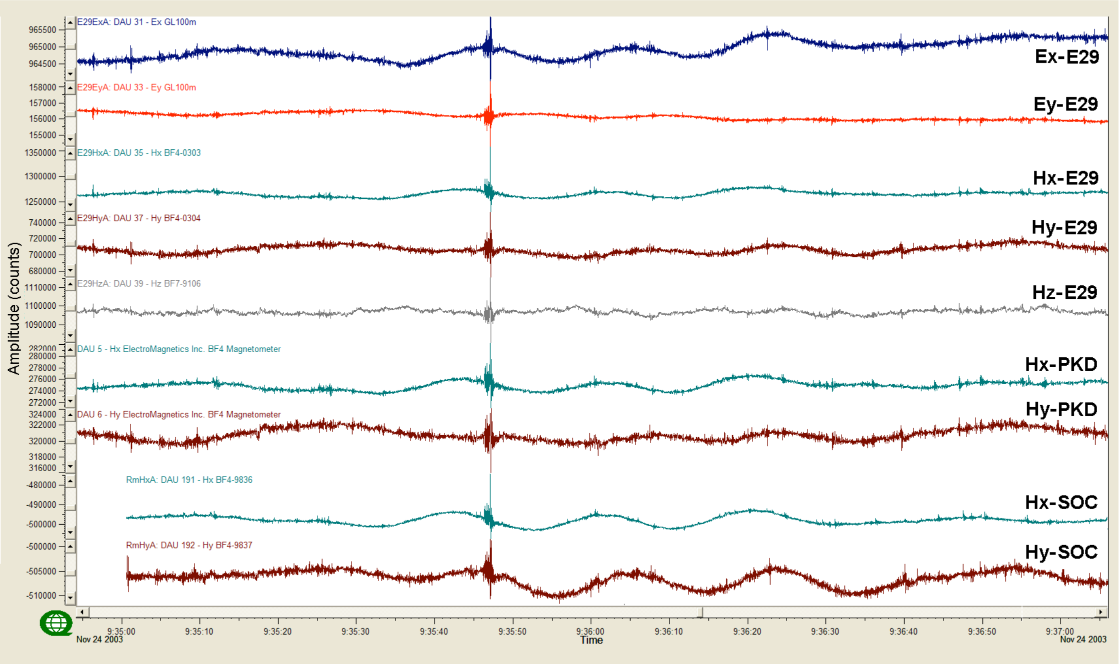

Figure 8. Comparison of all five channels of MT time series at site E29 with the two horizontal magnetic fields used as references at PKD and at SOC.

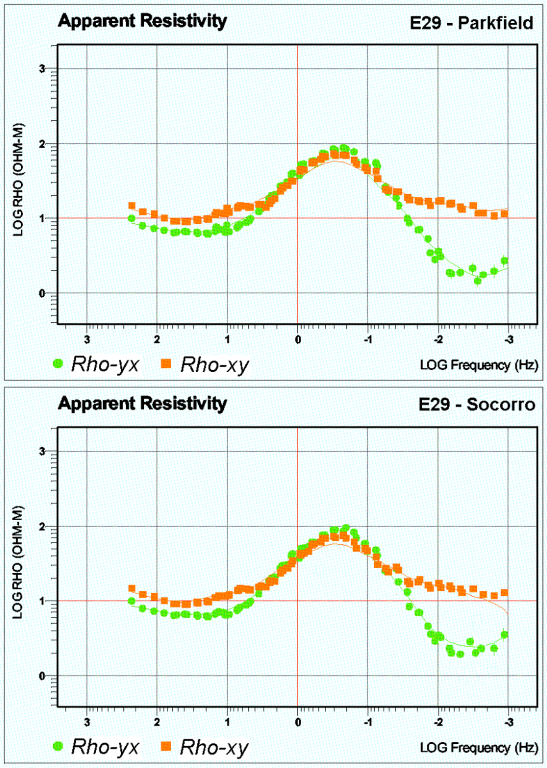

Figure 9. Sounding E29 processed using the Parkfield observatory as a reference compared to E29 (Figure 1) processed using the Socorro site as a reference.

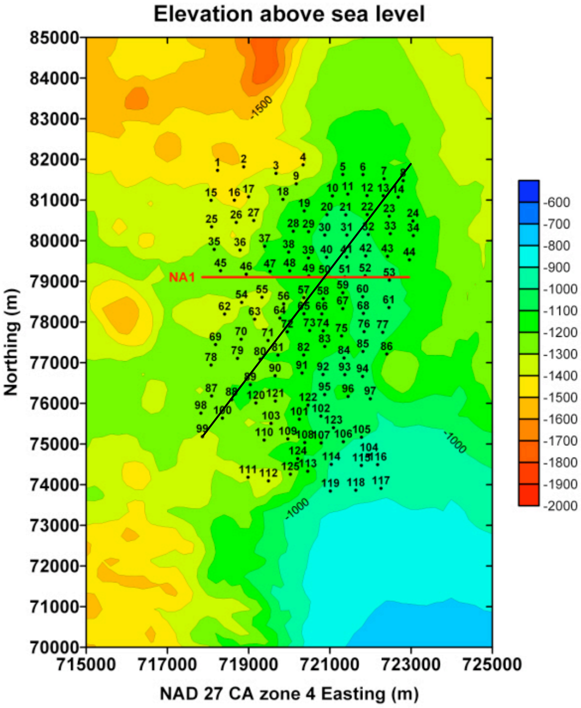

Figure 10. Coso MT site and elevation map in meters. NA1 is a contiguous bipole profile, Navy Array 1. Sites 1 to 102 were acquired in 2003 and sites 103 to 125 in 2005. Observed and predicted impedance data (apparent resistivity and phase) from the final 3D conductivity model will be compared along the oblique transect in Figure 18. The transect uses the following MT stations, starting at site 99, 99,100,88,89,71,72,65,50,41,32,22,13 and 8.

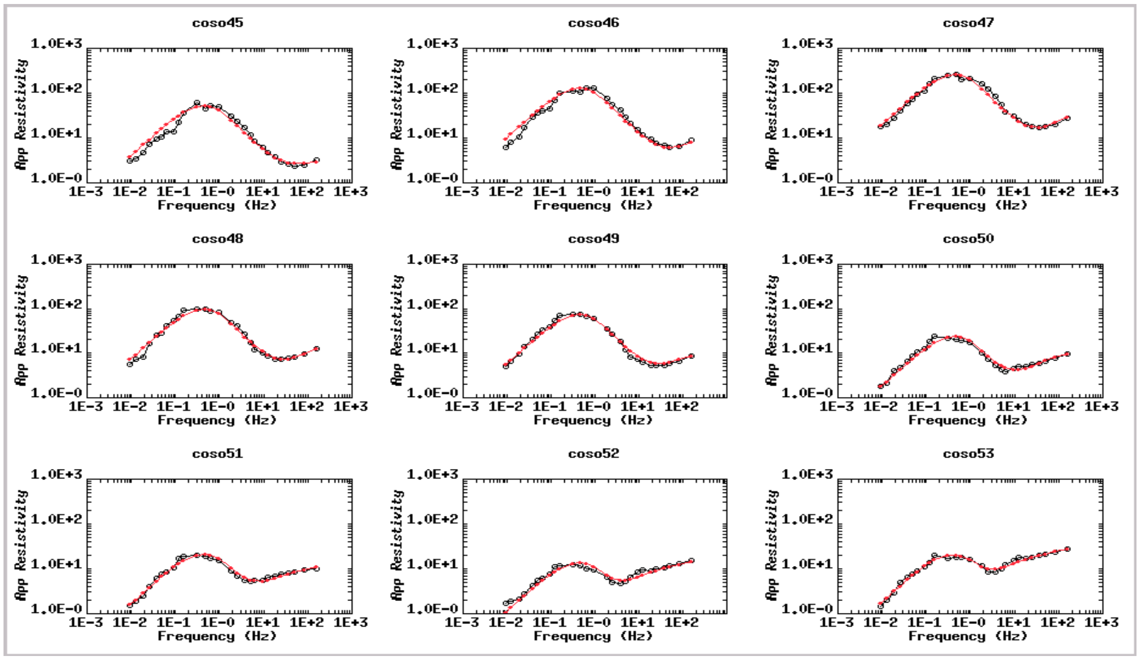

Figure 11. 2D TM fits to the Z_{yx} Coso data (apparent resistivity), where open circles represent the field data and red curves the model responses.

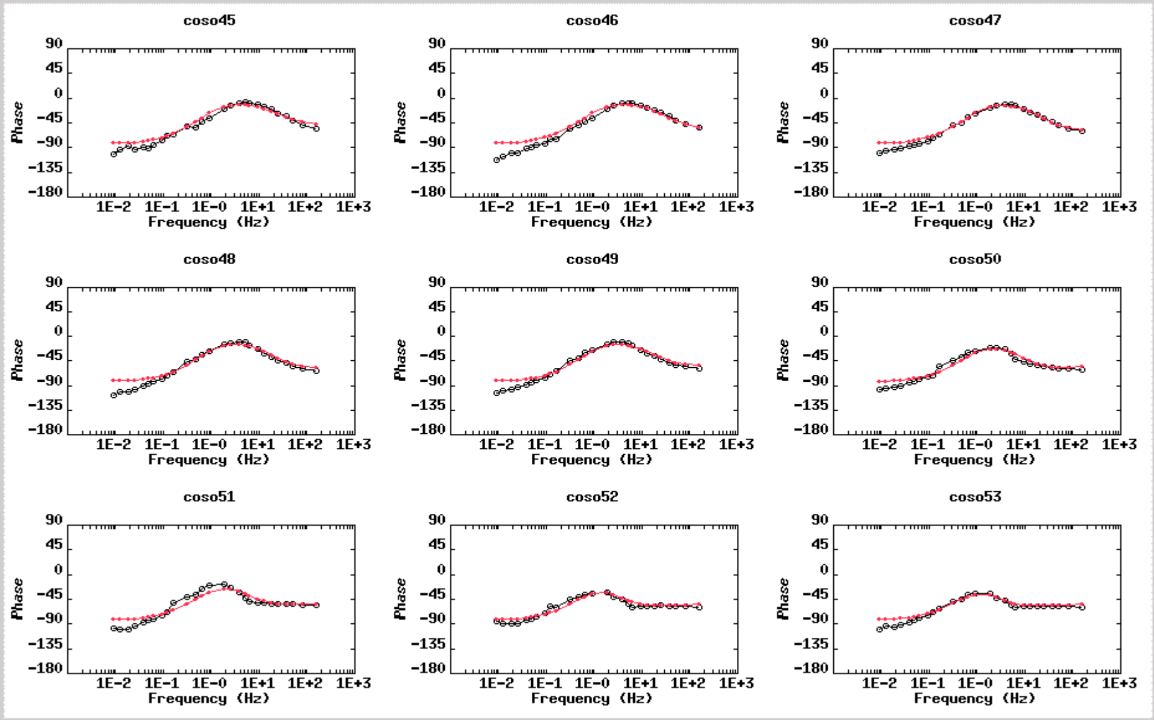
coso45
coso46
coso47
coso48
coso49
coso50
coso51
coso52
coso53
Phase
90
45
0
-45
-90
-135
-180
1E-2
1E-1
1E-0
1E+1
1E+2
1E+3
Frequency (Hz)

Figure 12. 2D TM fits to the Z_{yx} Coso data (impedance phase), where open circles represent field data and

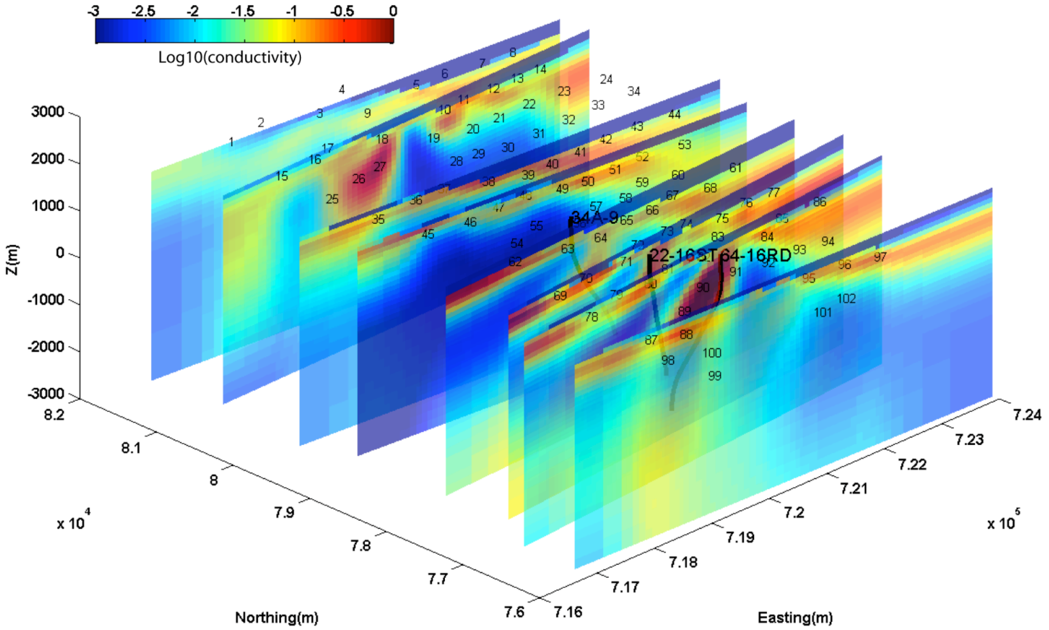

Figure 13. Starting conductivity model of the Coso geothermal site compiled from multiple 2D transects. Wells 64-16RD, 22-16ST and 34A-9 are also shown. The model view is from the southwest and includes site locations shown in Figure 10.

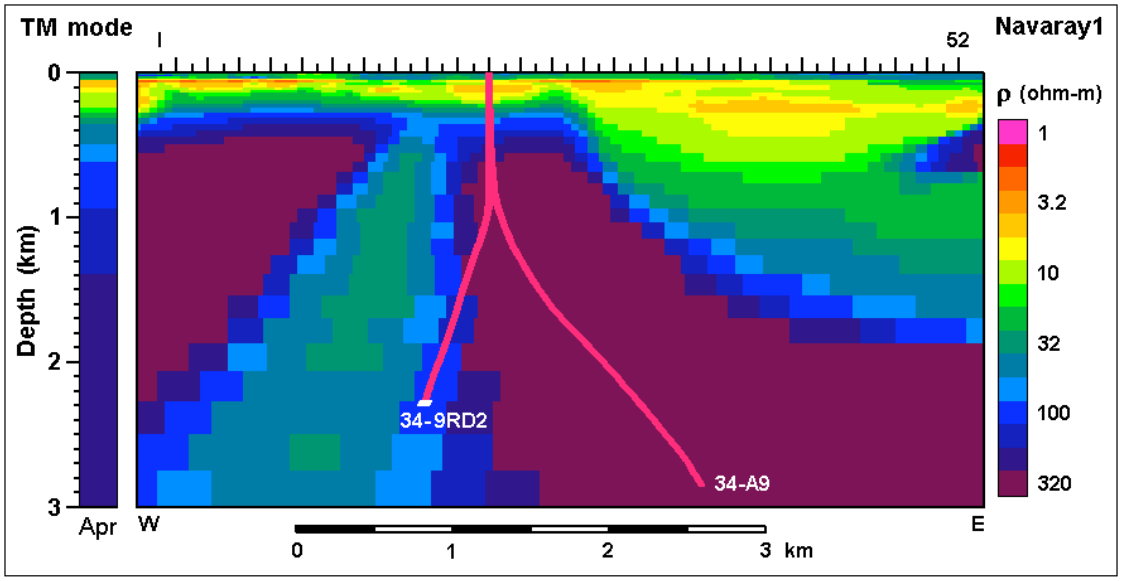

Figure14. 2D inversion model in resistivity (reciprocal of conductivity) using TM mode data of contiguous bipole profile NA1. Also plotted are deep wells 34-9RD2 and 34-A9 which project from about 500 m south of the profile. White patch at bottom of 34-9RD2 represents lost circulation zone. Inversion code used is based on forward problem of Wannamaker et al (1987) and jacobians of DeLugao and Wannamaker (1996), and damps variations from an average 1D a-priori model (Apr column on the left). This plot adopts warm colors for low resistivity. View is toward the north.

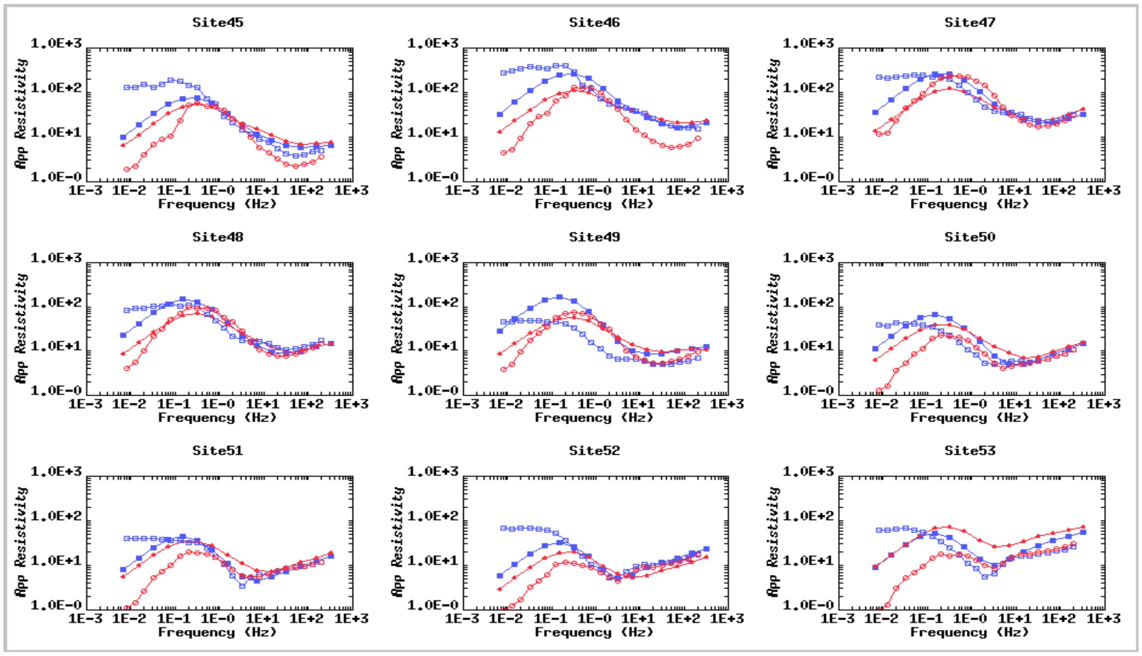

Figure 15. Comparison of apparent resistivity, for selected measurement sites 45-53, for the initial 3D starting model generated from interpolated 2D TM mode inversion. The blue curves with solid and open squares denote predicted and observed Z_{xy} apparent resistivity. The red curves, solid and open circles, denote predicted and observed Z_{yx} apparent resistivity.

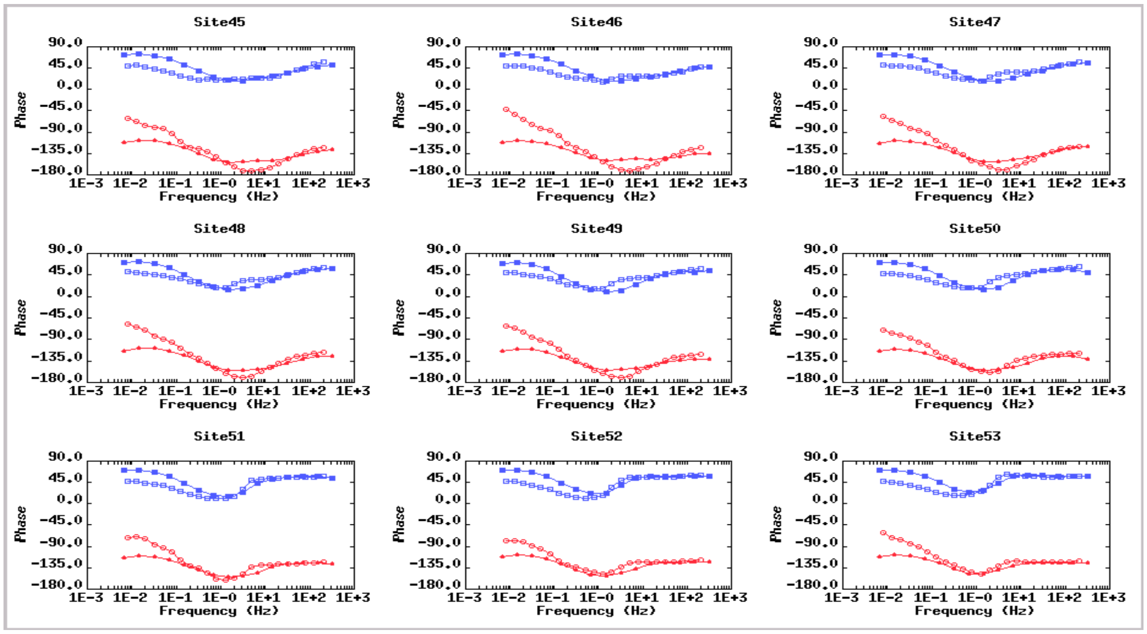

Figure 16. Comparison of impedance phase, for selected measurement sites 45-53, for the initial 3D starting model generated from interpolated 2D TM mode inversion The blue curves with solid and open squares denote predicted and observed Z_{xy} phase. The red curves, solid and open circles, denote predicted and observed Z_{yx} phase.

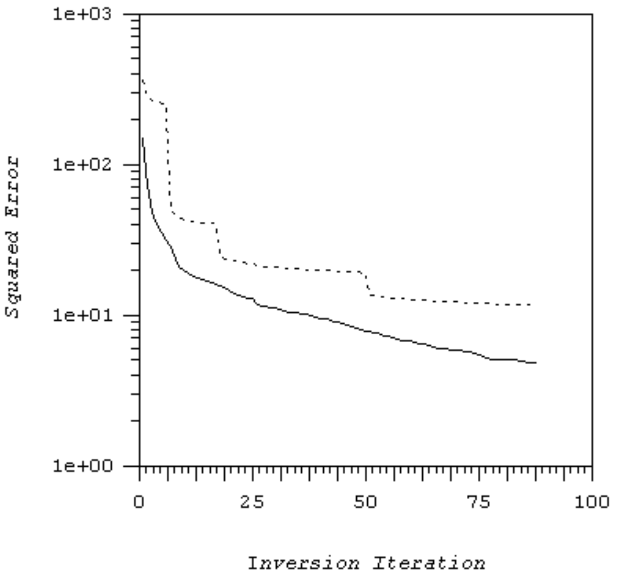

Figure 17. Plot of the convergence of the 3D inversion iteration for the 100 to 1 Hz data. The dashed curve is a plot of the convergence of the error functional with regularization constraint. The solid curve is a plot of the weighted squared error, the data misfit without regularization.

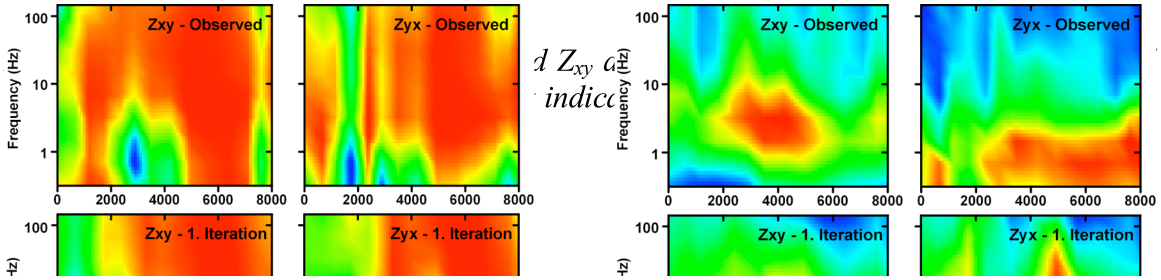

from the final 3D conductivity model based on the 2003 and 2005 data sets (100 to 0.3 S/m
Horizontal offsets in these plots are relative to site 99. Predicted results are shown for ıne
first and final inversion iteration showing the improvement obtained in the data fit.
elk

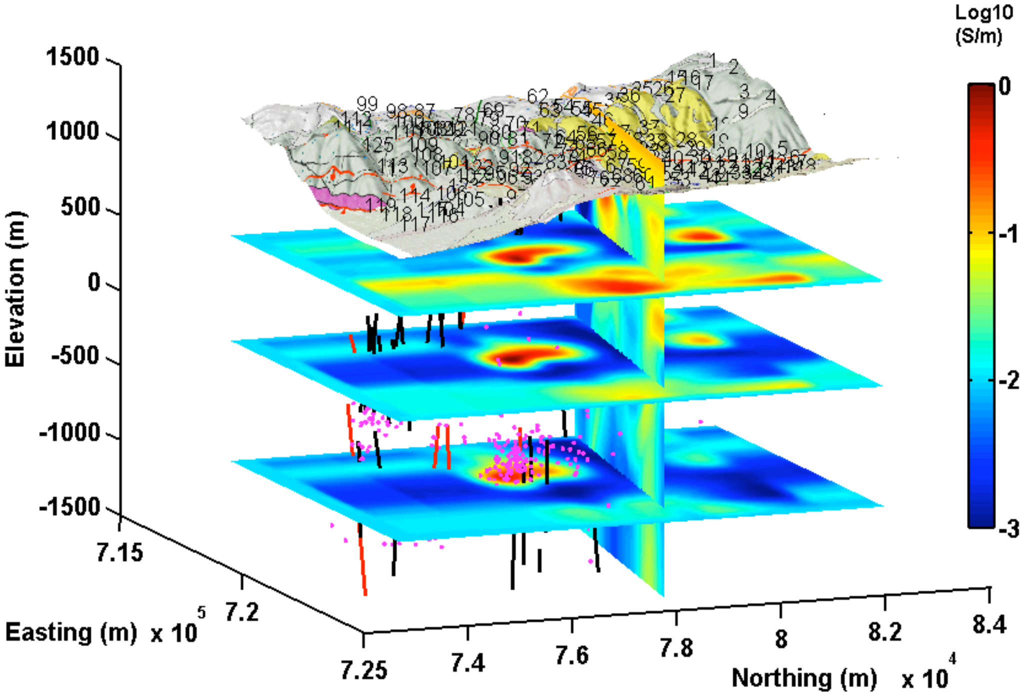

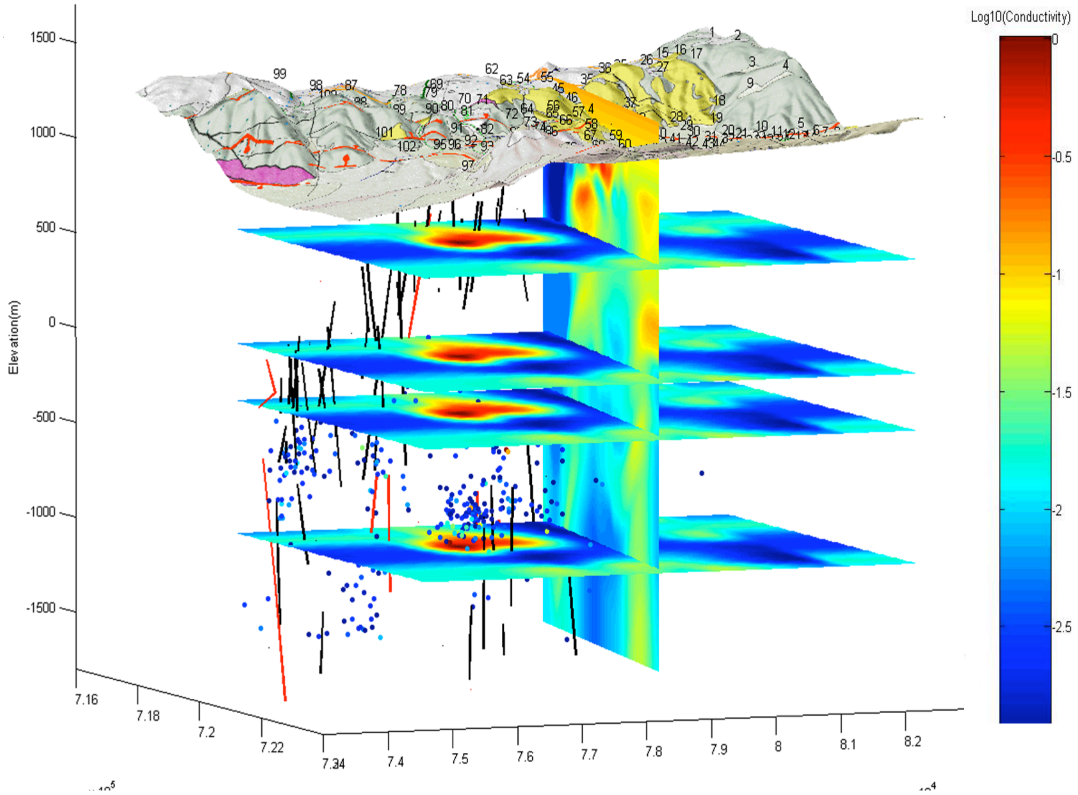

'e
n
's
o

0

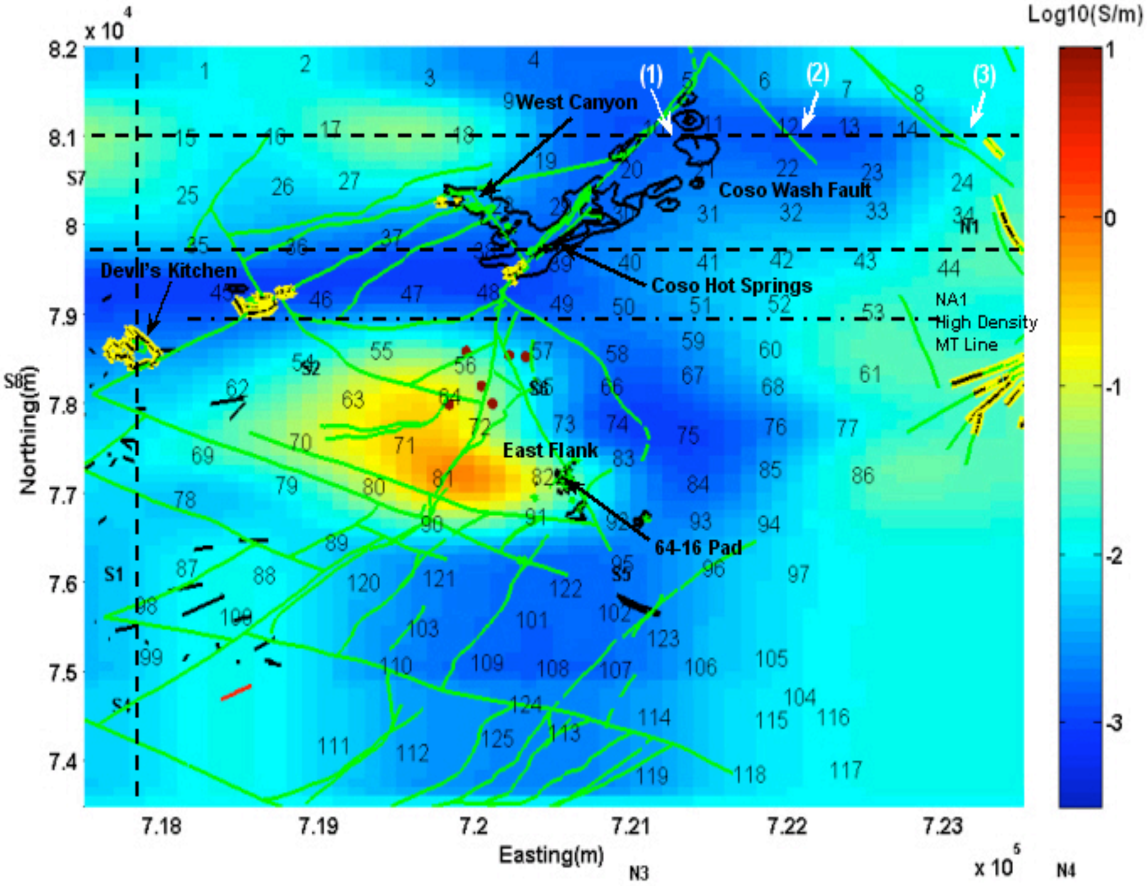

Figure 20. Horizontal slice through 3D conductivity model at a depth of 500m below sea-level based upon 2003 and 2005 data sets; 100 to 0.1 Hz. Color represent log10 of conductivity. The surface elevation averages 1200m above sea-level. Mapped surface expression of faulting are green liniments. The 125 MT stations are numbered. Micro-earthquake seismometer locations (S1, S2, S4, S5, S6, S7 and N1) from Lees and Wu (2000) are shown. Straight dashed lines are location of depth sections shown in Figures 21, 22 23 and 24. Location of the NA1 high-density MT line (Figure 10) is shown as the dot-dash horizontal black line near Northing 79,000 m.

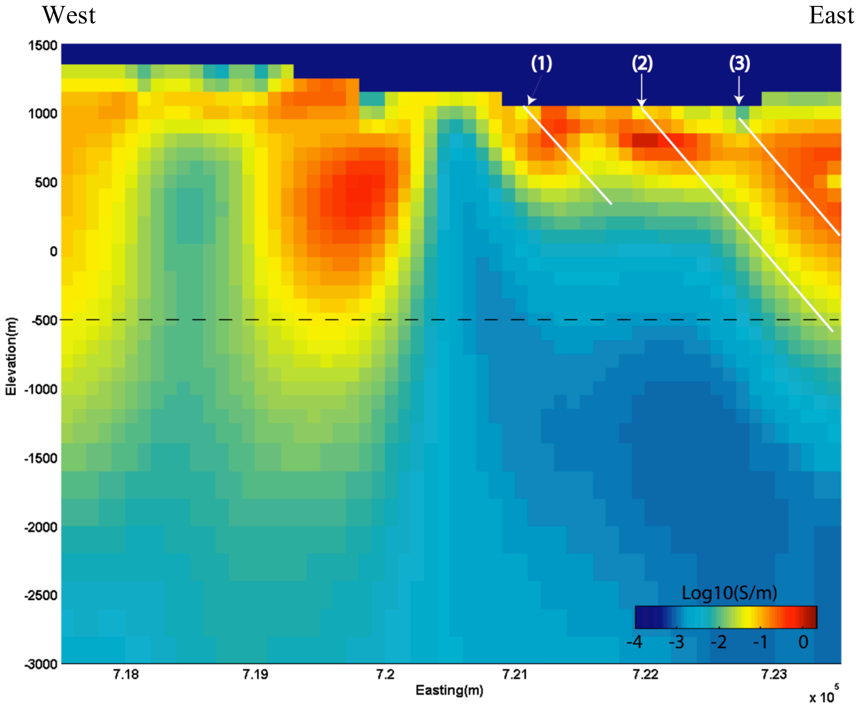

Figure 21. Vertical (west to east) cross-section at Northing 81,000. The fault marked (1) is the Coso Wash Fault, faults (2) and (3) are un-named and shown in plan view in Figure 20. The horizontal black dashed line is the level of the depth section shown in Figure 20.

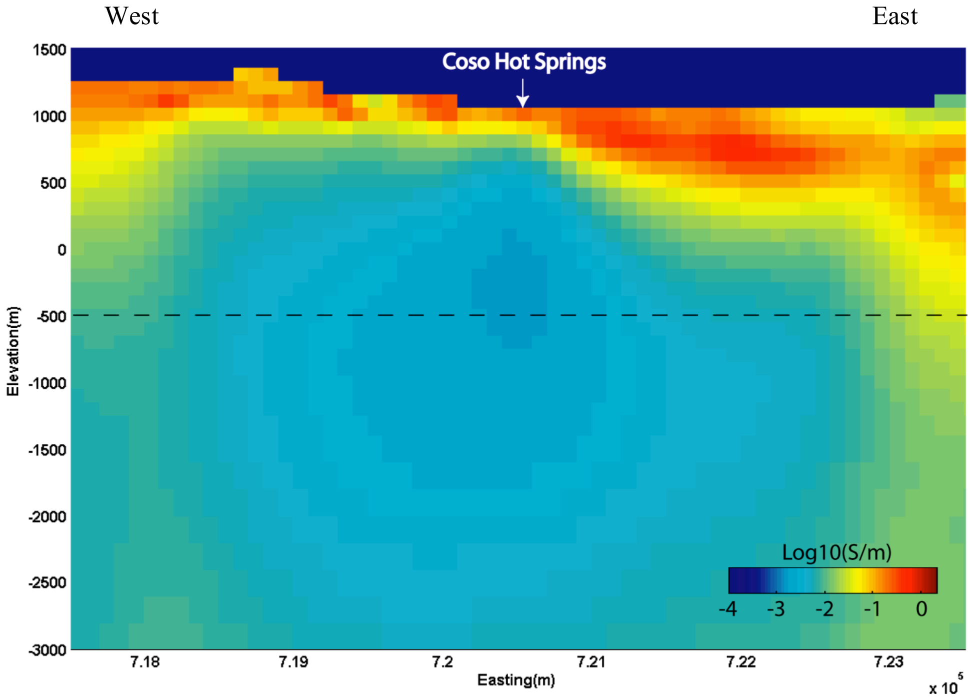

Figure 22. Vertical (west to east) cross-section at Northing 79,900. The section intersects Coso Hot Springs at the location shown. The horizontal black dashed line is the level of the depth section shown in Figure 20

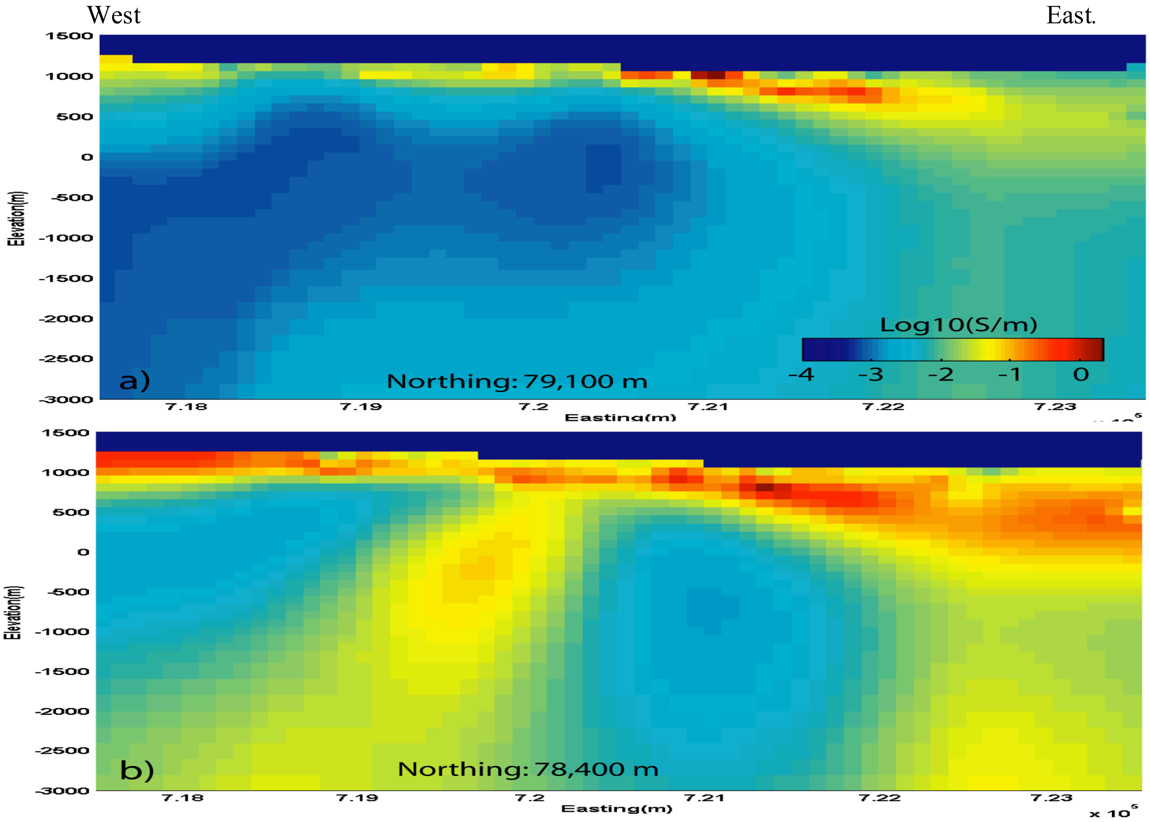

Figure 23. Vertical (west to east) cross sections at Northing 79,100 m (panel a) and Northing 78,400 m (panel b). The section in panel a) is at the location of the high-density MT line used to generate the 2D resistivity section shown in Figure 14; resistivity is the reciprocal of conductivity. The 2D inversion in Figure 14 appears to be responding to conductivity structure to the south. The vertical section through the 3D conductivity inversion 700 m to the south of the high-density line (panel b) is much closer to the 2D inverted result than is the section directly beneath the 2D line.

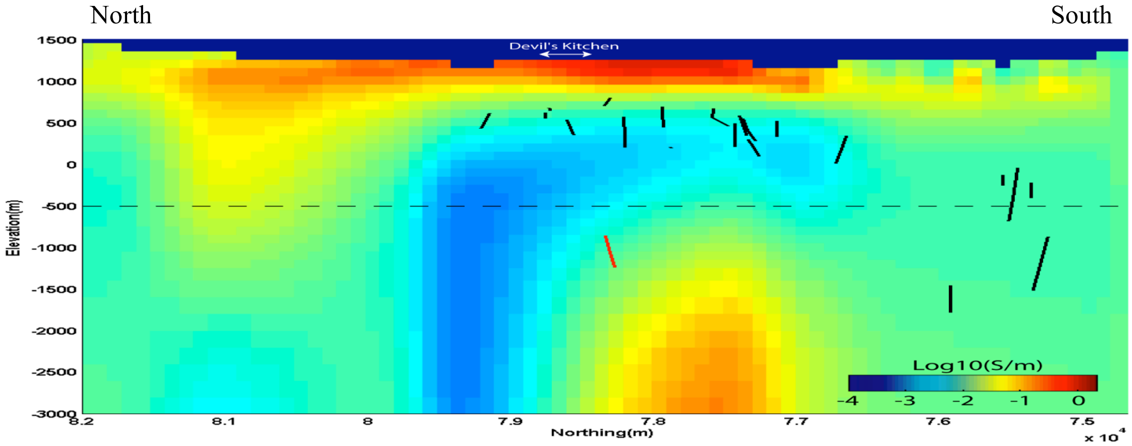

Figure 24. Vertical (north to south) section at Easting 717,900 m. The section intersects the Devil's Kitchen complex at the location shown. The horizontal black dashed line is the level of the depth slice

shown in Figure 20. The near vertical black line segments are the production interval's of wells near the

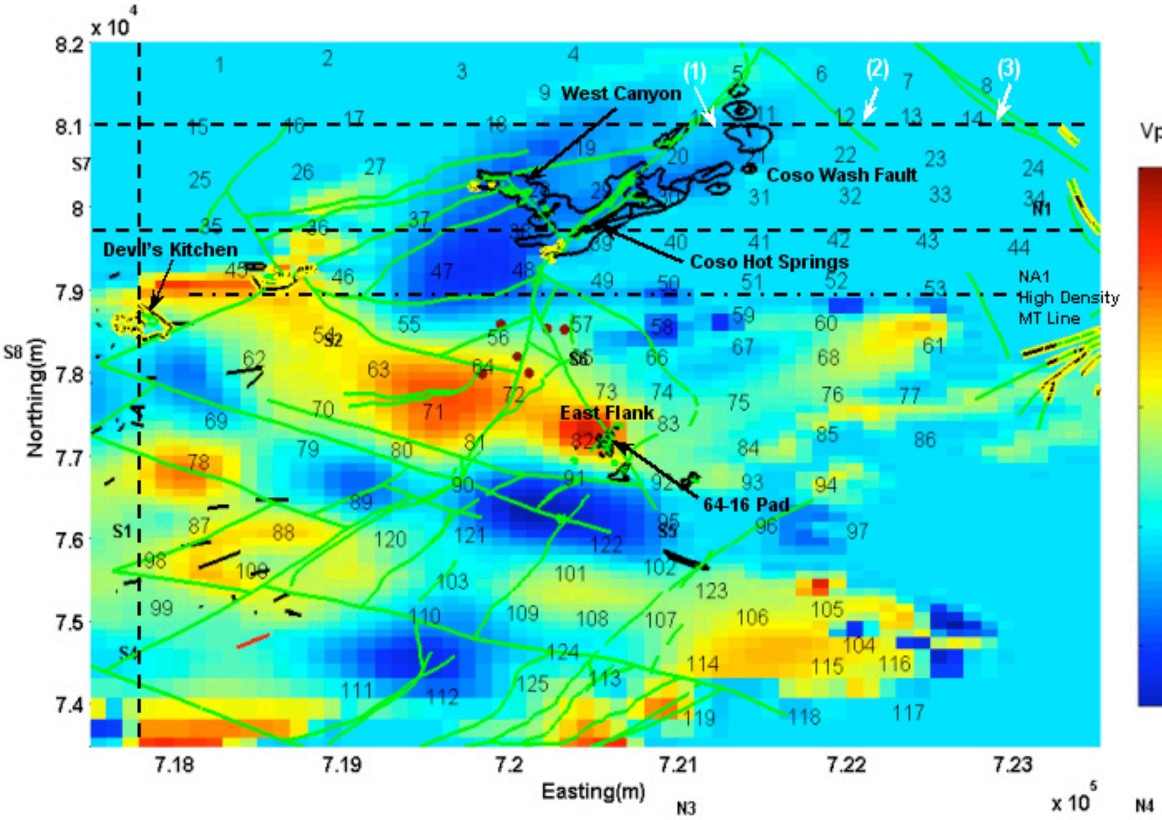

x 10^4
8.2
8.1
8
7.9
7.8
7.7
7.6
7.5
7.4
Northing(m)
7.18
7.19
7.2
7.21
7.22
7.23
Easting(m)
x 10^5
Vp/Vs
2.2
1.9
1.6
1.3
West Canyon
Coso Wash Fault
Coso Hot Springs
Devil's Kitchen
East Flank
64-16 Pad
NA1
High Density
MT Line
(1)
(2)
(3)
S1
S2
S3
S4
S6
S7
S8
N1
N3
N4

Figure 25. Horizontal slice through 3D MEQ derived velocity model from Lees and Wu (2000) (at a depth of 500m above sea-level. Color represent V_p/V_s ratio. The surface elevation averages 1200m above sea-level. Mapped surface expression of faulting are shown in green. The 125 MT stations are numbered. Micro-earthquake seismometer locations (S1, S2, S4, S5, S6, S7, S8 and N1) used for velocity tomography) are shown. Straight dashed lines are location of depth sections shown in Figures 21, 22, 23 and 24. Location of the NA1 high-density MT line is shown as the dot-dash horizontal black line near Northing 79,000 m.

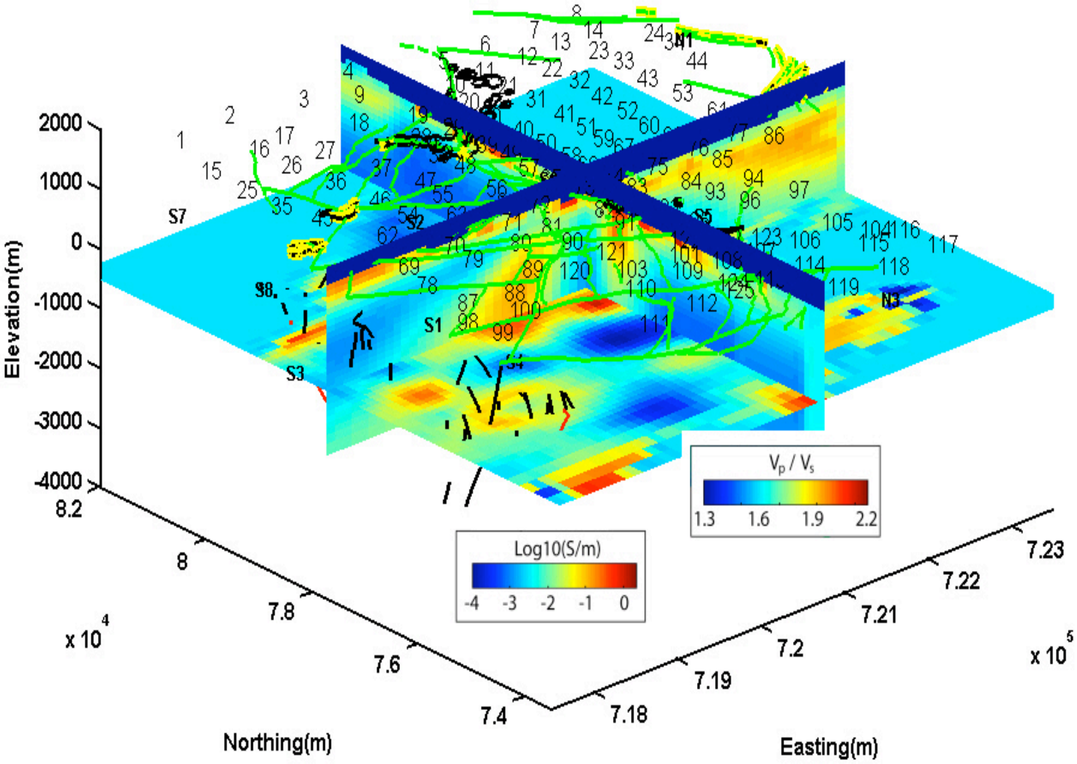

Figure 26. 3D view from the south-west of combined MT conductivity and MEQ velocity model. The vertical sections are log10 of conductivity and the horizontal slice is V_p/V_s ratio. Mapped surface expression of faults are green liniments. MT site locations are shown as numbers 1 to 125 and Micro-earthquake seismometer locations S1, S2, S4, S5, S6, S7, S8 and N1 used for velocity tomography are shown in bold font compared to the MT site numbers. Geothermal well production intervals are shown as near-vertical black lines while injection intervals are shown as near-vertical red lines.

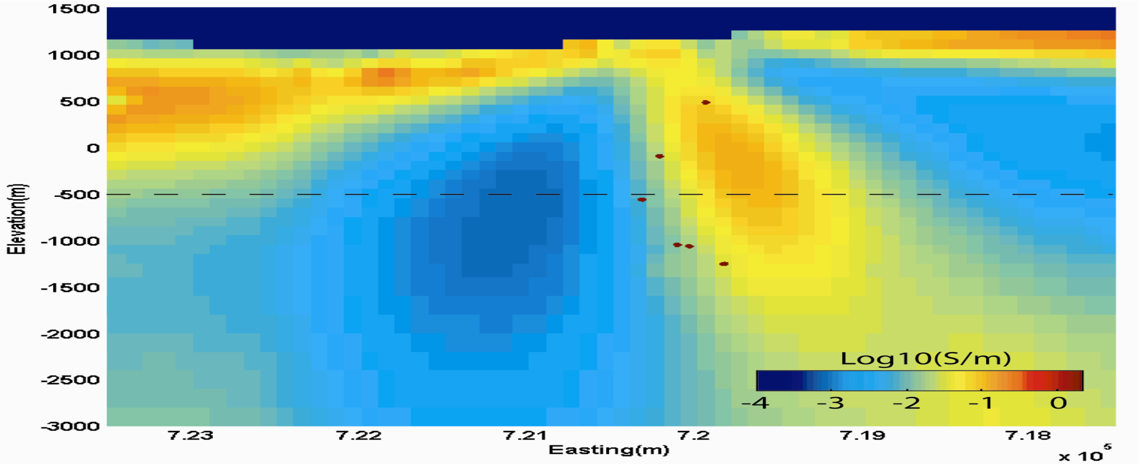

Figure 27. Depth section of 3D conductivity at Northing 77,900 m as viewed from the north. The locations of major mud loss into large open fractures are shown by black dots. All mud-loss locations are within 800m to the north of the section and are in the transition zone between high and low conductivity. The horizontal black dashed line shows the level of the horizontal section shown in Figure 20.